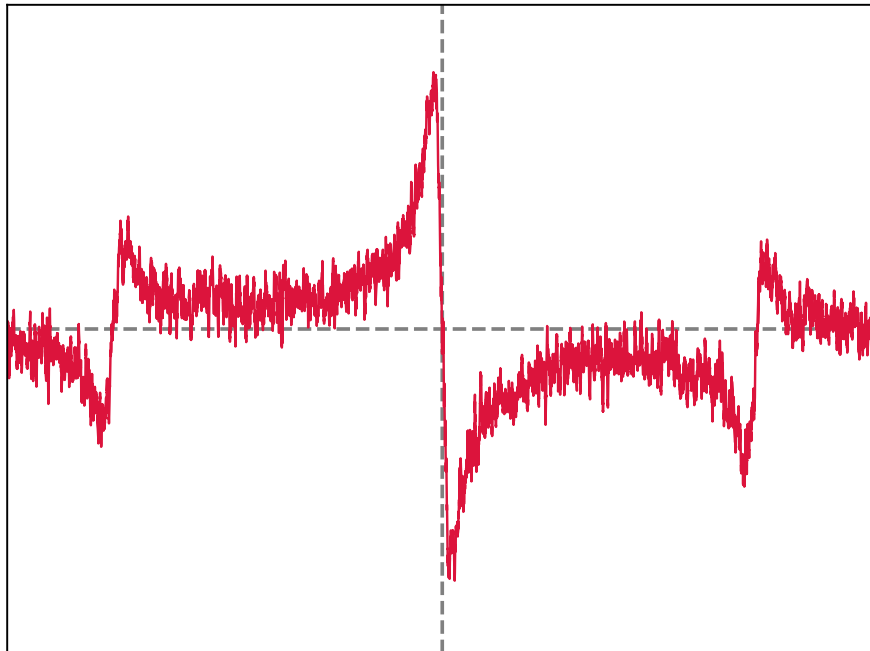


Design of a laser-locking system for $^{40}\text{Ca}^+$

Author: Simon Gartmann
Supervising Professor: Prof. Jonathan Home
Trapped Ion Quantum Information Group,
ETH Zürich
Supervisors: Roland Matt
Robin Oswald
Dr. Christopher Axline



August 29, 2019

Abstract

Trapped ions are a promising candidate for physical quantum computers. For experiments on $^{40}\text{Ca}^+$, we need stable lasers to interact consistently with the ion. The lasers we use cannot provide stable frequencies out of the box. Therefore we need a frequency-stabilization setup in order to get light we can use for our experiment. In this thesis we present optical cavities and associated locking electronics to stabilize laser frequencies. To correct laser frequency shifts, we use stable optical cavities and transfer this stability to the lasers using PDH-locking. The cavity mirrors are glued to a ULE glass block to be less susceptible to thermal fluctuations. Cavity resonance frequencies can be adjusted by changing cavity lengths using piezoelectric rings glued to one mirror of each cavity. This thesis further describes the design and assembly of the necessary electronics, which include a piezo driver and the electronics needed for PDH-locking. We have been able to couple 397 nm light into one of the cavities and confirmed the predicted cavity properties experimentally. Furthermore, we managed to use mostly commercially available components instead of custom-made parts.

Contents

1	Theory	2
1.1	Ion trapping	2
1.2	Gaussian optics	4
1.2.1	Laguerre-Gaussian modes	5
1.3	Optical cavities	6
1.4	PDH-locking	9
2	Electronics	17
2.1	Piezo electronics	17
2.1.1	Piezo characterization	20
2.2	Locking electronics (KILL)	21
3	Optics	23
3.1	Cavity design	23
3.2	Optics setup and mode-matching	24
4	Summary and Outlook	29
5	References	31
	Appendices	33
A	Mirror reflectivity plots	33
B	Electronics schematics	34
B.1	Piezo driving	34
B.2	KILL	36
B.3	Problems with KILL version 1.3.0	38
C	Procedures	39
C.1	Wire gluing	39
C.2	Mirror gluing	40
C.3	Beam alignment and mode-matching into cavity	40

Introduction

Quantum information and quantum computation have been fields of intense research in recent decades. Many different approaches to physically implement primitive quantum computers and quantum bits (qubits), one of them being trapped ions, have emerged as a consequence. David DiVincenzo [1] formulated a list of criteria a physical system needs to have in order to reach a fully functional quantum computer. Ions are a promising candidate as they have been shown to fulfill several of these criteria, with active research being conducted on the criteria that are not yet reached. They have long coherence times (order of seconds) compared to gate execution times (order of microseconds) and they can be manipulated with high fidelities both for state manipulation and readout [2, 3, 4, 5].

The ion is cooled to its ground state and put inside a vacuum to isolate it from thermal and mechanical noise. The electronic state is then manipulated using lasers to drive the desired transitions. The demands on the laser depend on what electronic transition it drives and the purpose of that transition. In the case of $^{40}\text{Ca}^+$, we use dipole-allowed transitions for state preparation, readout and Doppler cooling, while qubit gates use a dipole-forbidden transition. The latter has a linewidth of tenths of a Hertz, while the dipole-allowed ones have linewidths on the order of MHz. The unstabilized lasers we use can drift in frequency over time which is detrimental for driving these transitions, making frequency stabilization necessary. This can be achieved by building stable optical cavities as frequency references for the laser. In this thesis, we present a Pound-Drever-Hall-locking (PDH-locking, section 1.4) setup for locking four different lasers which will drive dipole-allowed transitions (details in section 1.1). This locking procedure transfers the stability of the cavity to stability of the laser. The implementation details are discussed in sections 2 and 3. The locking scheme detects the drift and applies the correction to the laser via an electronic feedback-loop.

In our group, there currently is one set of stabilized lasers for calcium which is shared between all experiments. So far this has worked well, but the setup is reaching its limits due to competition for power and different preferences for the exact working frequencies. Until now all the experiments have been in adjacent labs (B18, B20, B25) but with new experiments coming up in B108, it is desirable to have an additional set of stabilized lasers for calcium ions. This gives us more independence and flexibility, for example for driving different calcium isotopes such as $^{48}\text{Ca}^+$, which requires different frequencies. The new setup is compact and can fit on a single 600×600 mm breadboard, including all optics and an ion pump. Furthermore, we aim to use as little custom-built parts as possible and rely mostly on commercially available components for both electronics and optics.

1 Theory

This section is about the theory upon which the experimental work is based. First, I give a brief introduction to ion trapping for the specific case of $^{40}\text{Ca}^+$ including the electronic transitions relevant in this work and the experimental requirements for driving these transitions with lasers. Subsection 1.2 includes basic derivations and an overview of formulas of Gaussian optics and specifically Laguerre-Gaussian modes in 1.2.1. This is important for understanding coupling into cavities and optimizing mode-matching. Following that, subsection 1.3 is about optical cavities, their physical properties and it sets up the foundations for a laser frequency stabilization scheme called Pound-Drever-Hall-locking (PDH-locking). This method is described in more detail in subsection 1.4, where the working principle and physical parameters affecting it are explored in more detail. At the end of that section, the discussion shifts toward experimental limitations of PDH-locking. An introduction to quantum computation can be found in [5].

1.1 Ion trapping

This subsection is about the basics of ion trapping. I will go into specifics of electronic states of ions, the mechanisms of trapping and their use as qubits in quantum computing. The section gives an overview over the in-depth discussion from [6].

Ions are electrically charged and therefore they can be controlled using electromagnetic fields. There are different methods to keep ions spatially fixed, but here we focus on the approach using electric fields only. Static electric fields cannot form a stable trap due to Earnshaw's theorem, so this is circumvented using static fields in combination with fields oscillating at radio-frequencies. Massive particles such as ions have inertia which makes them react more slowly to applied forces. Since the field oscillations are fast, the ion sees the oscillating field as an effective trapping potential due to its inertia. These traps are called Paul traps, and there are different variants of them, such as Surface Electrode Traps (SET). More details on trap designs can be found in [6].

The ion in this case is $^{40}\text{Ca}^+$, which has a single valence electron. The energy level structure of the electron is shown in part in Fig. 1 with the atomic level notation $n^{2S+1}L_J$, where n is the principal quantum number, S is the spin angular momentum, L the orbital angular momentum and J is the total angular momentum. In the presence of a magnetic field, Zeeman-splitting lifts the degeneracy of these energy levels, which is also depicted in Fig. 1 for selected levels.

In principle, many states can be chosen as qubit states $|0\rangle$ and $|1\rangle$, here we use the ground state $4S_{1/2}$ and the metastable state $4D_{5/2}$. This $S - D$ transition with a wavelength of 729 nm is dipole-forbidden and therefore has a long lifetime of 1.05 s. This is useful in quantum computation since operations on the qubit can be performed in microseconds [5]. This means that on this qubit, many operations can be applied with a low chance of the qubit spontaneously decaying. The $P - D$ and $S - P$ transitions are both dipole-allowed and therefore have much shorter lifetimes. The $S - P$ transitions are used for cooling to the ground state and also for readout from the $4S_{1/2}$ state. On the other hand, the $D - P$ transitions are used for repumping the D -population to the S -state via the short-lived P -states. Repumping is used for resetting the qubit and also for catching the qubit, if the P

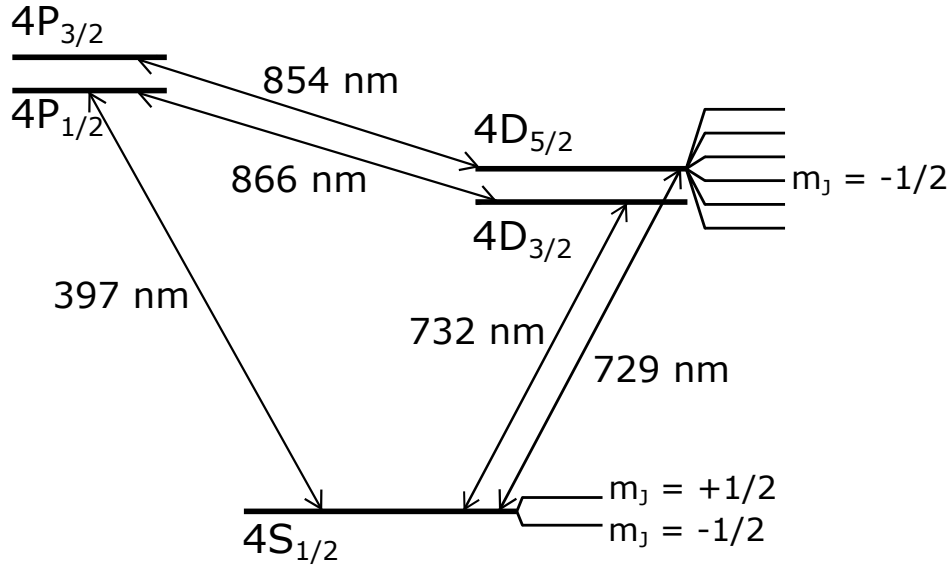


Figure 1: Electronic energy level structure of $^{40}\text{Ca}^+$ with transition wavelengths and selected Zeeman splittings. Figure adapted from [6].

state randomly decays to a D state instead of the ground state. Wavelengths λ , excited state lifetimes τ and transition linewidths Γ are summarised in Table 1 along with information on what each wavelength is used for.

The $^{40}\text{Ca}^+$ ion is prepared from neutral ^{40}Ca atoms via photoionization using 376 nm and 423 nm light. To achieve sufficiently low temperature to keep thermal excitations minimal, the ion then needs to be cooled. This ensures that the ion stays in the ground state and any excitations are well controlled via lasers. It also hinders the ion from escaping the trap and the electron from reaching higher energy states (“qubit leaking”). Doppler cooling can be used on the $S_{1/2} - P_{1/2}$ transition at 397 nm, since its lifetime is very short and the excitation decays quickly.

Transition linewidths determine how stable lasers driving these transitions have to be. Very narrow transitions such as the 729 nm $S - D$ transition require extremely stable lasers, as even tiny drifts or fluctuations are enough to make the laser unable to drive the transition. Frequency stabilization using a locking scheme is described in detail in subsection 1.4. Since the setup we show in section 3 is used to only lock frequencies we use for dipole-allowed transitions, the cavities we use for locking do not need to be as stable as for a dipole-forbidden transition such as 729 nm.

λ [nm]	τ [ns]	Γ [2π MHz]	Purpose
397	7.7	20.7	State preparation and readout, Doppler cooling
729	1.05×10^9	1.52×10^{-7}	Qubit rotation
854	94.3	1.69	Repumping
866	101	1.58	Repumping
732	1.08×10^9	1.47×10^{-7}	For future work
423	4.49	35.4	Photoionization, MOT

Table 1: Overview over state transitions relevant in this thesis. Values of state lifetime τ and transition linewidths Γ taken from [6, 7]. Magneto-optical traps (MOT) can be used to cool and trap neutral atoms [8].

1.2 Gaussian optics

Gaussian optics is a part of optics which deals with Gaussian intensity distributions. They are important in the context of this work, since the laser used all produce close to Gaussian beams. In particular, this section is about the spatial evolution of these beams and how they transform when passing through optical elements such as lenses. Gaussian beams are useful for these considerations since Gaussian beams stay Gaussian for basic optical elements, only their parameters change. At the end, Laguerre-Gaussian modes are introduced since they are important for cavity-coupling in our setups [9].

First, I will give an overview over the basic derivation steps and the main results following [10]. In this part, we focus on the spatial evolution of Gaussian beams along their path. Under this condition the general wave equation

$$\left[\frac{1}{c^2} \frac{\partial^2}{\partial t^2} - \vec{\nabla}^2 \right] u = 0$$

reduces to the Helmholtz equation using a separation of variables where we discard the time-dependent part

$$\begin{aligned} u(\vec{r}, t) &= A(\vec{r}) T(t) , \\ \implies \left[\vec{\nabla}^2 + k^2 \right] A(\vec{r}) &= 0 . \end{aligned}$$

In the step from the wave equation to the Helmholtz equation, the wave number $k = \frac{2\pi}{\lambda}$ is introduced. Since we are also dealing with beams and not point sources, the Helmholtz equation further simplifies into its paraxial form

$$\vec{\nabla}_{\perp}^2 + 2ik \frac{\partial A}{\partial z} + 2k^2 A = 0 , \quad (1)$$

where z is the direction of beam propagation and $\vec{\nabla}_{\perp}^2$ stands for the divergence perpendicular to the direction of propagation z .

Gaussian beams are solutions of the paraxial Helmholtz equation and their general form is given by

$$\vec{E}(r, z) = E_0 \hat{x} \frac{w_0}{w(z)} e^{\frac{-r^2}{w(z)^2}} \exp \left[-i \left(kz + k \frac{r^2}{2R(z)} - \psi(z) \right) \right] , \quad (2)$$

where r is the radial distance from the z -axis, E_0 the electric field amplitude, k is the wave number, $R(z)$ is the curvature of the wavefront at z and $\psi(z)$ is the so-called Gouy phase. The terms $w_0 = w(z = 0)$ and $w(z)$ describe the beam waist. In this thesis, the term waist describes the radius at which the beam intensity falls to $\frac{1}{e^2}$ of the value at the center of the beam unless specified otherwise. These properties of Gaussian beams can be written as

$$\text{Rayleigh range : } z_R = \frac{\pi w_0^2}{\lambda}, \quad (3)$$

$$\text{Beam waist : } w(z) = w_0 \sqrt{1 + \left(\frac{z}{z_R}\right)^2}, \quad (4)$$

$$\text{Wavefront curvature : } R(z) = z \left[1 + \left(\frac{z_R}{z}\right)^2\right], \quad (5)$$

$$\text{Gouy phase : } \psi(z) = \arctan\left(\frac{z}{z_R}\right).$$

The Rayleigh range z_R is the distance along the beam where the on-axis intensity is half the peak intensity. It is wavelength dependent and therefore the evolution of waist and curvature of the beam are also dependent on the wavelength λ . Note that the paraxial approximation only holds for beams that do not strongly diverge, i.e. $w_0 \gg \lambda$, which is the case in the setups presented in section 3.

1.2.1 Laguerre-Gaussian modes

Modes are particular solutions of the Helmholtz equation which form an orthogonal basis for Gaussian intensity distributions. In free-space propagation of Gaussian beams they are not relevant in this thesis, but when a beam couples into a cavity, only certain spatial modes are supported by the cavity. Cavity modes will be discussed in more detail in subsection 1.3. In the setup presented in section 3, spherical mirrors form the cavity, therefore we choose to work in a cylindrical coordinate system. In this coordinate system, the modes are called Laguerre-Gaussian modes [9, 11]. Fig. 2 shows a few ideal low-order Laguerre-Gaussian modes as well as pictures taken of cavity modes.

Transverse Laguerre-Gaussian modes are described by two indices, usually called l and p , which correspond to azimuthal and radial order of the mode. Assuming the beam is propagating along the z -axis, the mode field amplitude is described by

$$E(r, \phi, z) = C_{lp} \frac{w_0}{w(z)} \left(\frac{\sqrt{2} r}{w(z)}\right)^{|l|} e^{-\frac{r^2}{w^2(z)}} L_p^{|l|}\left(\frac{2r^2}{w^2(z)}\right) \exp\left[-ik\frac{r^2}{2R(z)} - il\phi + i\psi(z)\right],$$

where L_p^l are generalized Laguerre polynomials, C_{lp} is a normalization constant, $w(z)$ and $R(z)$ are defined as in eq. 4 and 5 and $\psi(z)$ is the adjusted Gouy phase [11]

$$C_{lp} = \sqrt{\frac{2p!}{\pi(p+|l|)!}},$$

$$\psi(z) = (2p + |l|) \arctan\left(\frac{z}{z_R}\right).$$

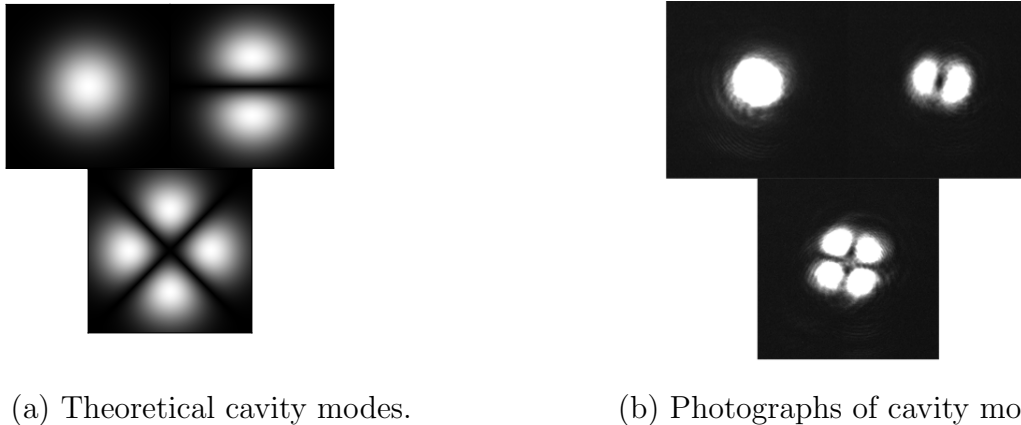


Figure 2: Comparison of real Laguerre-Gaussian modes to computer-generated ideal modes. Panel (a) shows computer-generated mode intensities inside the cavity. In panel (b) are photographs taken using a CMOS-camera¹ set up on the transmission side of the cavity. We used 397 nm light to couple into the cavity. The camera is saturated, therefore the intensity gradients appear differently compared to the ideal modes.

1.3 Optical cavities

Optical cavities (also called resonators or etalons) consist of two or more mirrors, set up in a way that allows light to form a standing wave. Their main uses are in lasers, where they surround the gain medium, and in interferometers. However, in this case they will be used as a frequency reference for frequency-stabilization of lasers. The stability of the optical cavity will be transferred to stability of the laser's frequency via a feedback loop. Inside a resonator, only resonant frequencies can form standing waves, off-resonant light will interfere destructively [9]. This section gives an overview of the relevant physical properties needed for frequency-stabilization through PDH-locking.

In this setup four long-radius hemispherical cavities [9], each consisting of one flat and one spherical mirror, were used. The term long-radius stems from the fact that the curvature of the curved mirror is longer than the cavity length in this configuration. How well light can be confined in a cavity can be characterized by the stability condition

$$0 \leq g_1 g_2 \leq 1, \quad (6)$$

where each mirror has a stability parameter defined using the cavity length L and a mirror's radius of curvature R as

$$g_i = 1 - \frac{L}{R_i}. \quad (7)$$

The stability condition in particular necessitates that either none or both of the involved stability parameters g_i are negative, which has to be considered when designing a cavity.

The spectral behaviour of cavities is periodic in frequency. This period is called the free spectral range $\Delta\nu_{\text{FSR}}$. It is defined as

¹Firefly MV FMVU-03MTM

$$\Delta\nu_{\text{FSR}} = \frac{c_m}{2L}, \quad (8)$$

where c_m is the speed of light in the medium inside the cavity and L is the length of the cavity. The free spectral range depends solely on the geometry of the cavity. Depending on the use case, this may therefore also be an important factor in cavity design, e.g. for interferometry.

Since real mirrors are not perfectly reflecting, there is not only one exact frequency that is on resonance, but the cavity has a resonance linewidth. This is shown in Fig. 3 for mirrors with 99% reflectivity. The linewidth determines the spectral resolution of a cavity and the full-width-half-maximum linewidth can be calculated as

$$\Delta\nu_{\text{FWHM}} = -\frac{\Delta\nu_{\text{FSR}}}{2\pi} \ln(R_1 R_2). \quad (9)$$

Here, R_1 and R_2 are the reflectivities of the two cavity mirrors. For perfectly reflective mirrors, the linewidth would be zero and the resonance spectrum would be a series of delta peaks [12]. Furthermore, imperfections such as contamination of mirror surfaces and other losses can also lead to broadened linewidths.

The last resonator property discussed in this work is the finesse. It is defined as

$$\mathcal{F} = \frac{\Delta\nu_{\text{FSR}}}{\Delta\nu_{\text{FWHM}}} = -\frac{2\pi}{\ln(R_1 R_2)} \quad (10)$$

and it combines free spectral range and cavity linewidth. The finesse can be seen as a measure of quality of the cavity, in the sense of high finesse cavities being closer to a theoretically perfect cavity with perfectly reflecting mirrors. High finesse cavities have a smaller linewidth and therefore higher spectral resolution, which can be crucial depending on the use case [12].

Light confined in a cavity will be reflected many times by the mirrors and thus interfere with itself constantly inside the cavity. The consequence of this is that most frequencies interfere destructively, but certain patterns are allowed. For cylindrical systems as ours, these patterns are Laguerre-Gaussian modes, introduced in 1.2.1. Light can only couple into these discrete modes of the cavity. Weak coupling leads to significant loss of signal intensity, which for most applications of cavities is detrimental. It is due to insufficient overlap of the real beam with the cavity mode and can have many causes, including angular and translational misalignment, off-resonant frequency, mismatched beam waist and mismatched wavefront curvature [13]. However, good coupling into a single mode leads to experimentally getting very close to the theoretical cavity properties.

When the light's frequency is on resonance with the cavity, the light leaking out from the cavity will destructively interfere with the light reflected on the in-coupling mirror, resulting in no visible reflection from the cavity. We can write this using the reflection coefficient

$$F(\omega) = \frac{E_{\text{ref}}}{E_{\text{inc}}}, \quad (11)$$

where ω is the light's frequency and E_{inc} is the incoming electric field amplitude. E_{ref} is the total reflected field amplitude, see Fig. 4 (b) for a schematic depiction of all contributing factors. It can be calculated as a geometric sum of all reflections from the cavity.

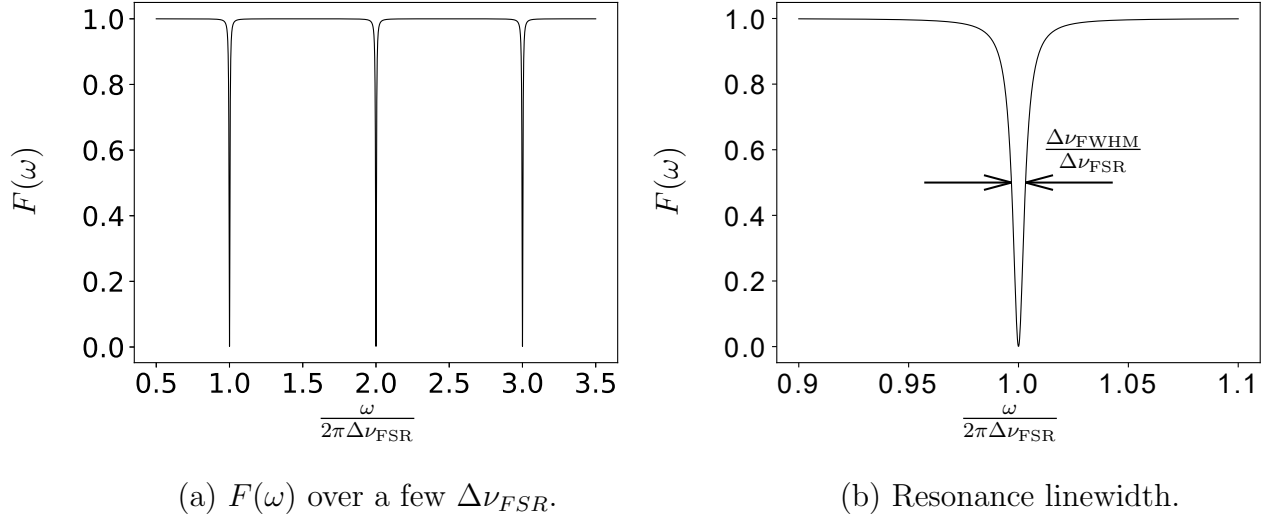


Figure 3: Plots of the reflection coefficient over several free spectral ranges (a) and linewidth demonstration for a cavity with $\Delta\nu_{\text{FSR}} = 1$ GHz, $\mathcal{F} \approx 312$ and $\Delta\nu_{\text{FWHM}} \approx 3.2$ MHz (b). Both plots use the same cavity parameters.

In this discussion, Fresnel coefficients r, t, r' and t' to describe reflection and transmission on mirrors will be used [14]. The coefficients r and t describe reflection and transmission from one side of the mirror, whereas r' and t' describe the same for the opposite direction. Implicitly, these coefficients are dependent on the angles of incidence, but this is not relevant in this treatment. This convention is visualized in Fig. 4. This leads to the following expression for the reflected light, using $\phi = \frac{\omega}{\Delta\nu_{\text{FSR}}}$

$$\begin{aligned}
 \frac{E_{\text{ref}}}{E_{\text{inc}}} &= r + tr't'e^{i\phi} + t(r')^3t'e^{2i\phi} + t(r')^5t'e^{3i\phi} + \dots \\
 &= r + tt'r'e^{i\phi} [1 + (r')^2e^{i\phi} + (r')^4e^{2i\phi} + \dots] \\
 &= r + tt'r'e^{i\phi} \frac{1}{1 - (r')^2e^{i\phi}}.
 \end{aligned}$$

At this point we use Stokes' relations [14] for Fresnel coefficients,

$$\begin{aligned}
 r' &= -r \\
 r^2 + tt' &= 1,
 \end{aligned}$$

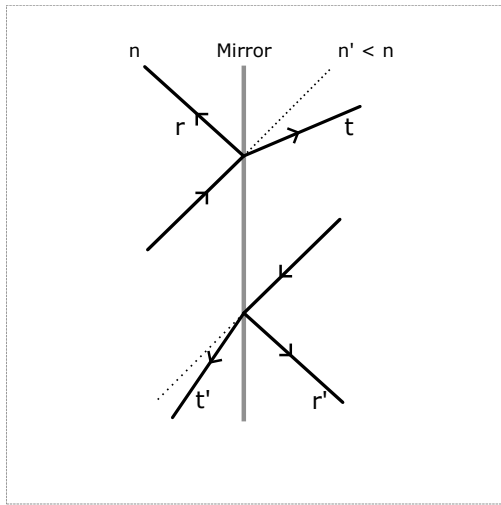
to simplify the expression for the reflection coefficient and express it only in terms of r' as this is the coefficient conventionally used to describe mirror reflectivities. Note that r and r' can be defined arbitrarily but in this thesis, all definitions are consistent with the schematic in Fig. 4 (a). This results in the following calculation:

$$\begin{aligned}
F(\omega) &= \frac{E_{\text{ref}}}{E_{\text{inc}}} = (-r') \left[1 - \frac{(1-r^2)e^{i\phi}}{1-(r')^2e^{i\phi}} \right] \\
&= (-r') \left[\frac{1-r^2e^{i\phi} - e^{i\phi} + r^2e^{i\phi}}{1-(r')^2e^{i\phi}} \right] \\
&= r' \frac{e^{i\phi} - 1}{1-(r')^2e^{i\phi}} = r \frac{1 - e^{i\phi}}{1 - r^2e^{i\phi}} , \\
&= r \frac{1 - e^{i\frac{\omega}{\Delta\nu_{\text{FSR}}}}}{1 - r^2e^{i\frac{\omega}{\Delta\nu_{\text{FSR}}}}} .
\end{aligned} \tag{12}$$

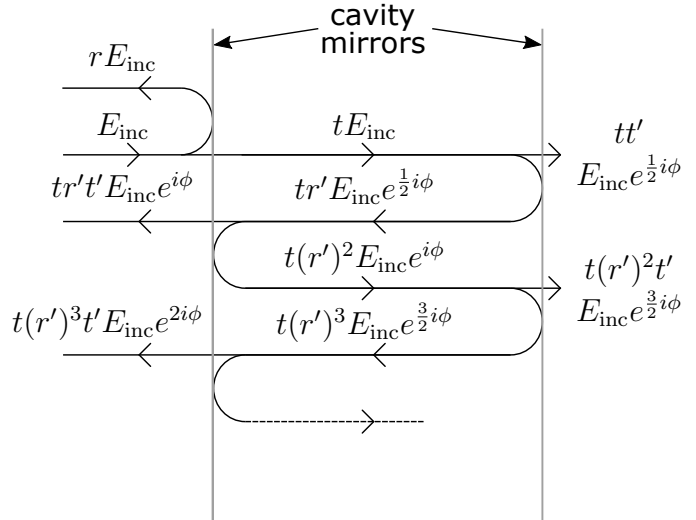
For a frequency on resonance with the cavity, the reflection coefficient becomes zero and no reflection can be observed:

$$F(\omega = 2\pi n\Delta\nu_{\text{FSR}}) = 0, \text{ for any integer } n ,$$

and for off-resonant frequencies, the reflection coefficient is non-zero, as depicted in Fig. 3 (a).



(a) Fresnel coefficients.



(b) Fabry-Pérot schematic.

Figure 4: Illustrations of Fresnel coefficients and components for the reflection coefficient. Panel (a) gives a visual guideline to how the coefficients are defined in the context of this thesis. Panel (b) shows in detail where the beam picks up which coefficients and phases while it makes roundtrips in a Fabry-Pérot cavity. The principle holds in the same way for cavities with curved mirrors.

1.4 PDH-locking

Lasers of any kind are subject to thermal effects and other sources of noise, such as electronic noise or vibrations, which lead to frequency and intensity fluctuations and drifts over time. The interactions of light with ionic electronic states are sensitive to the frequency of light

and experiments in quantum computation require high stability over time. Therefore it is inevitable to stabilize the laser using a locking technique. A well established method of locking a laser is based on the work of R. V. Pound, R. W. P. Drever and J. L. Hall and it uses a very stable cavity as a frequency reference [15, 16, 17]. The principle behind locking is that the stability of the cavity gets transferred to stability of laser frequency. This subsection goes through the mathematics of phase modulation and how it can be used to stabilize laser frequencies. Afterwards, experimental implementation and limits are discussed.

The reflection from a cavity is a good way to check if the laser frequency is on resonance with the cavity. If the laser drifts, the reflection increases as described in the previous chapter and Fig. 3. However, from simply measuring reflected intensity it is impossible to know whether the laser frequency increased or decreased, which prevents immediate correction. Such a scheme is called top-of-range-locking. An alternative is side-of-range-locking, where one aims to lock to a frequency slightly off-resonance. Then, one can infer the direction of the drift from whether the reflection signal increases or decreases. But in side-of-range-locking, intensity fluctuations are indistinguishable from frequency fluctuations. PDH-locking therefore utilizes light modulation and the fixed phase relation between carrier and sidebands to determine the direction of any drifts, which allows that distinction. It also is not susceptible to intensity fluctuations.

Here, we look at phase modulation, but modulation of other properties follows the same principles. Until this point, only spatial evolution of Gaussian beams was discussed, but now we look at time-dependent intensities. This introduces complex phases, which are important for looking at interference of light, which is essential for understanding the locking procedure. Phase modulation transforms the beam $E_0 e^{i\omega t}$ with angular frequency ω and amplitude E_0 into the modulated beam

$$E_{\text{mod}} = E_0 e^{i\omega t} e^{\beta \sin(\Omega t)} = E_0 e^{i(\omega t + \beta \sin(\Omega t))} ,$$

where β is the modulation depth, a measure of the strength of modulation, and Ω is the modulation frequency. In PDH-locking, the focus is on the carrier and first sidebands, assuming low modulation depth β , which can be observed easily in a Jacobi-Anger expansion [18] of the modulated beam

$$\begin{aligned} E_{\text{mod}} &= e^{i\omega t} \left[J_0(\beta) + \sum_{n=1}^{\infty} i^n J_n(\beta) \sin(n\Omega t) \right] \\ &\approx E_0 e^{i\omega t} [J_0(\beta) + 2iJ_1(\beta) \sin(\Omega t)] \\ &= E_0 [J_0(\beta) e^{i\omega t} + J_1(\beta) e^{i(\omega+\Omega)t} - J_1(\beta) e^{i(\omega-\Omega)t}] . \end{aligned}$$

In the last step in the calculation above, the identity $2i \sin(\phi) = e^{i\phi} - e^{-i\phi}$ was used. This approximation is valid for $\beta \leq 1$, otherwise higher order Bessel functions, i.e. sidebands, contribute significantly. Fig. 5 shows plots of Bessel functions J_n (Panel (a)) and the corresponding sideband powers $|J_n|^2$ (Panel (b)). Moving from the amplitude picture to looking at the intensity or power of the light, we observe the following split of total power into sideband and carrier power

$$\begin{aligned}
P_0 &= |E_0|^2, \\
P_c &= J_0^2(\beta)P_0, \\
P_s &= J_1^2(\beta)P_0, \\
\implies P_0 &\approx P_c + 2P_s.
\end{aligned} \tag{13}$$

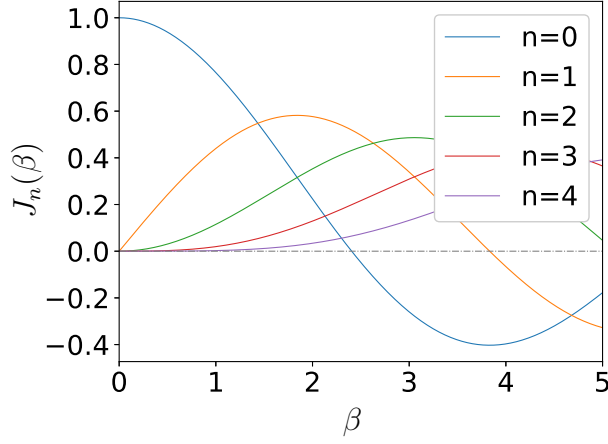
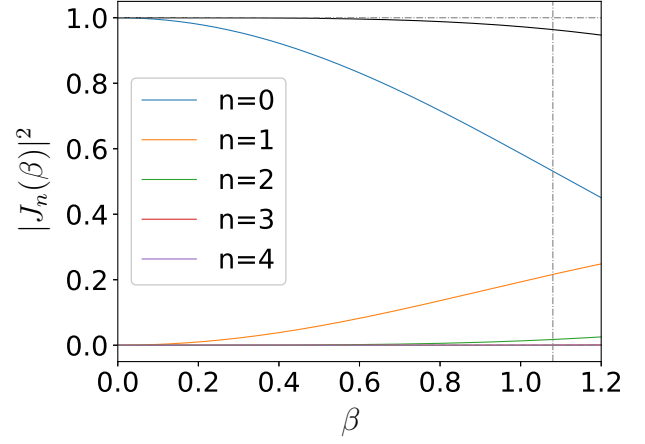
(a) First few Bessel functions J_n .(b) Corresponding powers $|J_n|^2$.

Figure 5: Bessel functions J_n up to 4th order (a) and Power in carrier and first few sidebands (b) up to $\beta = 1.0$. The black curve in (b) corresponds to combined power in carrier and first sidebands. It serves as a visual validation that the approximations we make hold in the regime $\beta \leq 1$. The vertical line at $\beta = 1.08$ indicates the value at which the error signal is most sensitive. This is discussed later in the section.

This modulated beam is then coupled into the cavity and the reflection from the cavity is described by

$$E_{\text{ref}} = E_0 \left[F(\omega)J_0(\beta)e^{i\omega t} + F(\omega + \Omega)J_1(\beta)e^{i(\omega+\Omega)t} - F(\omega - \Omega)J_1(\beta)e^{i(\omega-\Omega)t} \right], \tag{14}$$

which gives the expression for total reflected power:

$$\begin{aligned}
P_{\text{ref}} &= |E_{\text{ref}}|^2 = E_{\text{ref}}E_{\text{ref}}^* \\
&= |F(\omega)|^2 J_0^2(\beta)P_0 \\
&\quad + J_1^2(\beta)P_0 \left[|F(\omega + \Omega)|^2 + |F(\omega - \Omega)|^2 \right] \\
&\quad + J_0(\beta)J_1(\beta)P_0 \left\{ [F(\omega)F^*(\omega + \Omega) - F^*(\omega)F(\omega - \Omega)]e^{-i\Omega t} \right. \\
&\quad \left. + [F^*(\omega)F(\omega + \Omega) - F(\omega)F^*(\omega - \Omega)] \right\} + 2\Omega \text{ terms.}
\end{aligned}$$

$$\begin{aligned}
&= P_c |F(\omega)|^2 + P_s |F(\omega + \Omega)|^2 + |F(\omega - \Omega)|^2 \\
&\quad + \sqrt{P_c P_s} \left\{ [F(\omega)F^*(\omega + \Omega) - F^*(\omega)F(\omega - \Omega)] e^{-i\Omega t} \right. \\
&\quad \left. + [F^*(\omega)F(\omega + \Omega) - F(\omega)F^*(\omega - \Omega)] \right\} + 2\Omega \text{ terms.} \\
&\approx P_c |F(\omega)|^2 + P_s [|F(\omega + \Omega)|^2 + |F(\omega - \Omega)|^2] \\
&\quad + 2\sqrt{P_c P_s} \left\{ \Re [F(\omega)F^*(\omega + \Omega) - F^*(\omega)F(\omega - \Omega)] \cos(\Omega t) \right. \\
&\quad \left. - i \Im [F(\omega)F^*(\omega + \Omega) - F^*(\omega)F(\omega - \Omega)] i \sin(\Omega t) \right\} + 2\Omega \text{ terms.} \tag{15}
\end{aligned}$$

The 2Ω terms are due to sideband-sideband interactions. In the last transformation, the identity $e^{ix} = \cos(x) + i \sin(x)$ was used.

The term we want to isolate from this reflection signal is the last one,

$$i \Im [F(\omega)F^*(\omega + \Omega) - F^*(\omega)F(\omega - \Omega)] i \sin(\Omega t) ,$$

as this will be the one that allows us to determine the direction of the drift. The isolation of this term can be done via mixing of this reflected power with the modulation signal. A fast enough photodiode is used to convert this optical power into an analog signal, which can then be mixed with the analog modulation signal. Depending on the delay between modulation and measurement of the reflection, there can be a phase-shift between the two signals which can be corrected using a phase shifter. Mathematically, frequency mixing corresponds to multiplication of the two signals²

$$P_{\text{error}} = P_{\text{ref}} \times \sin(\Omega t) .$$

After mixing, the result will be passed through a low-pass filter which results in many terms being dropped in this calculation. Any 2Ω terms will leave behind oscillating terms and therefore they do not need to be considered any further. Terms from equation 15 involving $\cos(\Omega t)$ are also dropped, since $\sin(0) = 0$ and the additive term is oscillating. Therefore, only the terms including $\sin(\Omega t)$ survive the low-pass filter after mixing:

$$P_{\text{error}} = 2\sqrt{P_c P_s} \Im [F(\omega)F^*(\omega + \Omega) - F^*(\omega)F(\omega - \Omega)] . \tag{16}$$

This is called the error signal power P_{error} .

The carrier frequency should be near resonance and the modulation frequency should be designed to be large enough that the sidebands are decidedly off-resonance. In this case it is reasonable to assume that the sidebands are totally reflected, $F(\omega \pm \Omega) \approx 1$. Then the error signal power simplifies to

²Two trigonometric identities are useful for converting this product into the final error signal

$$\begin{aligned}
\sin(\omega t) \sin(\omega' t) &= \frac{1}{2} [\cos((\omega - \omega')t) - \cos((\omega + \omega')t)] , \\
\sin(\omega t) \cos(\omega' t) &= \frac{1}{2} [\sin((\omega - \omega')t) + \sin((\omega + \omega')t)] .
\end{aligned}$$

$$\begin{aligned}
F(\omega)F^*(\omega + \Omega) - F^*(\omega)F(\omega - \Omega) &\approx 2i \Im\mathfrak{m}[F(\omega)] , \\
P_{\text{error}} &\approx 4\sqrt{P_c P_s} \Im\mathfrak{m}[F(\omega)] =: \epsilon .
\end{aligned}
\tag{17}$$

This is called the Pound-Drever-Hall error signal ϵ . An ideal error signal is plotted in Fig. 6.

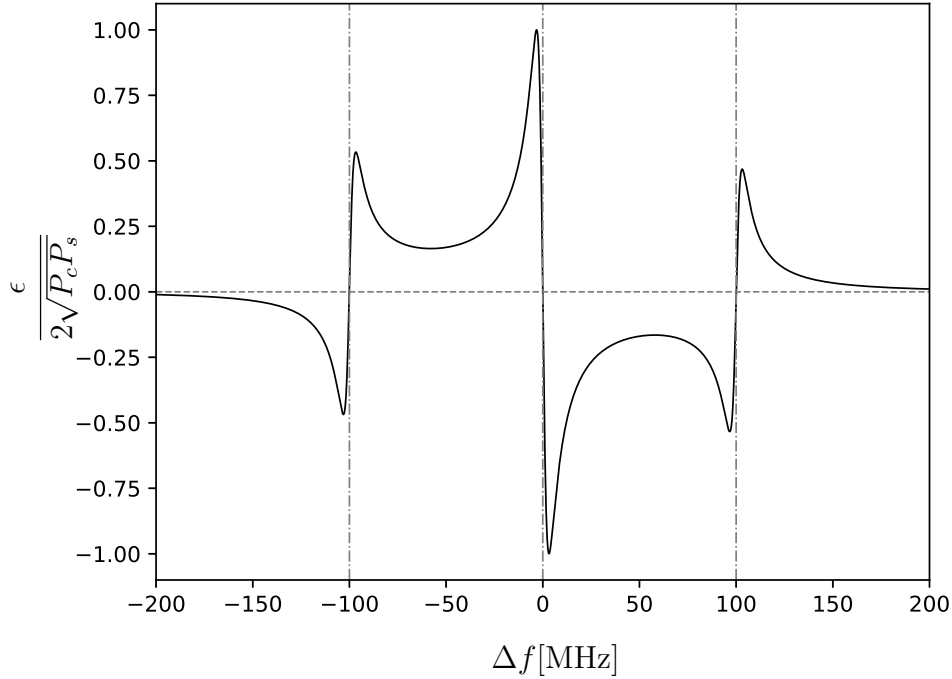


Figure 6: Ideal PDH-error signal for $\frac{\Omega}{2\pi} = 100$ MHz, $\beta = 1.0$ plotted against the detuning from resonance Δf . The cavity in this case has a free spectral range $\Delta\nu_{\text{FSR}} = 1$ GHz and a finesse $\mathcal{F} = 312$. The exact shape of the error signal is determined by many factors, but it is also not relevant. The important features are the linear slope around the center and the range where the sign of the signal stays the same on either side of resonance. This range is determined by the modulation frequency (dotted lines).

Assuming high finesse cavities and sidebands far off resonance, the following simplifications can be made:

$$\begin{aligned}
\mathcal{F} &= \frac{\pi}{1 - r^2} = \frac{\Delta\nu_{\text{FSR}}}{\Delta\nu_{\text{FWHM}}} \\
\omega &= 2\pi n \Delta\nu_{\text{FSR}} + \delta\omega, n \in \mathbb{Z} \\
\implies F(\delta\omega) &= -\frac{i}{\pi} \frac{\delta\omega}{\Delta\nu_{\text{FWHM}}} ,
\end{aligned}$$

and thus the PDH-error signal from eq. 17 becomes

$$\epsilon = -4 \frac{\sqrt{P_c P_s}}{\pi} \frac{\delta\omega}{\Delta\nu_{\text{FWHM}}} = -8 \frac{\sqrt{P_c P_s}}{\Delta\nu_{\text{FWHM}}} \delta f . \quad (18)$$

The actual locking range is determined by the sign of ϵ , and therefore by the modulation frequency. For example, a detuning of -50 MHz in the setup of Fig. 6 results in a positive ϵ and it will be corrected by increasing the laser frequency, which moves the laser towards resonance with the cavity. However, a detuning of 150 MHz results in a negative ϵ , which leads to a decrease of laser frequency, which further moves the light from resonance. In this case, the locking has failed. The ideal locking range is the linear part of the signal around resonance $\delta f = 0$. Its slope is described by a proportionality constant, the so-called frequency discriminant

$$D \approx - \frac{8\sqrt{P_c P_s}}{\Delta\nu_{\text{FWHM}}} , \quad (19)$$

which depends also on the cavity linewidth $\Delta\nu_{\text{FWHM}}$. The error signal ϵ around resonance is then described by the linear relation

$$\epsilon = D \delta f . \quad (20)$$

The error signal slope D also indicates how sensitive the error signal is to changes in laser frequency. The value of D depends on the power in carrier and sidebands. Since these values are given by the modulation depth β , so is D . The highest sensitivity is given by choosing $\beta = 1.08$, which corresponds to a power split $P_s = 0.42 P_c$.

Using PDH-locking, the frequency of the laser can be stabilized to within fractions of a cavity linewidth. Higher finesse cavities results in a tighter lock, but they are experimentally harder to couple into and lock to, as is evident by a steeper frequency discriminant in the error signal for smaller linewidths. The stability of the cavity also limits the effective linewidth of the lock. If the cavity drifts due to thermal or other effects, the laser might still be locked to the cavity, but now to an unstable frequency. Electronic noise in signal processing can also negatively affect the lock. Most noise can be optimized, but ultimately one is limited by shot noise. In the end, noise from all sources is indistinguishable from frequency noise. Shot noise is Poissonian noise and scales with the inverse square root of the number of incident particles, in this case photons [19, 20]

$$P_{\text{SN}} = \frac{P_{\text{PD}}}{\sqrt{N}} , \quad N = \frac{2\lambda}{hc} P_{\text{PD}} ,$$

where P_{PD} is the power incident on the photodiode, N is the number of photons reaching the photodiode and P_{SN} is the amount of shot noise. Near resonance, we can assume that only the sidebands contribute to the power that is reflected by the cavity onto the photodiode

$$P_{\text{PD}} = 2P_s \implies P_{\text{SN}} = \sqrt{\frac{4hc}{\lambda}} P_s ,$$

The signal-to-noise ratio (SNR) of the error signal near resonance is then, using eq. 20,

$$\begin{aligned}
\text{SNR} &= \left| \frac{\epsilon}{P_{\text{SN}}} \right| = \left| \frac{D \delta f}{\sqrt{\frac{2hc}{\lambda} P_s}} \right|, \\
&= \frac{\delta f}{\Delta\nu_{\text{FWHM}}} \sqrt{\frac{8\lambda P_c}{hc}}.
\end{aligned} \tag{21}$$

Note that the SNR only depends on carrier power P_c , not the power in the sidebands P_s . The shot-noise-limited frequency resolution can then be calculated by inverting eq. 21 and setting $\text{SNR} = 1$

$$\delta f_{\text{min}} = \Delta\nu_{\text{FWHM}} \sqrt{\frac{hc}{4\lambda P_c}}.$$

For a typical power of $P_c = 1$ mW, $\lambda = 397$ nm and $\Delta\nu_{\text{FWHM}} = 4$ MHz, the frequency resolution is $\delta f = 44.7\mu$ Hz. This gives a fundamental limit on the resolution of the lock, but experimentally, other noise sources limit the resolution further than this. These factors include electronic noise from the locking electronics, thermal effects on optics and the cavity and mechanical vibrations which disturb the optics.

In practice, the signals from the photodiode and the modulation signal might be out of phase depending on electronic delays in the diode and in cables. This can be fixed using a phase shifter, for example between the oscillator and the modulator. Since the mixing should happen using the modulation frequency, the output from the oscillator needs to be split between the modulator and the mixer. The output from the mixer is then fed into a PID (proportional-integral-derivative) controller, which applies the correction to the laser. Fig. 7 shows a setup of the essential elements needed for this locking method. In our group, these electronics are combined on a single custom-made PCB, called KILL (Keitch-Integrated-Laser-Lock) after its designer Ben Keitch [21]. The error signal is then read out by a PID controller which then shifts the carrier frequency in the laser closer to resonance [19].

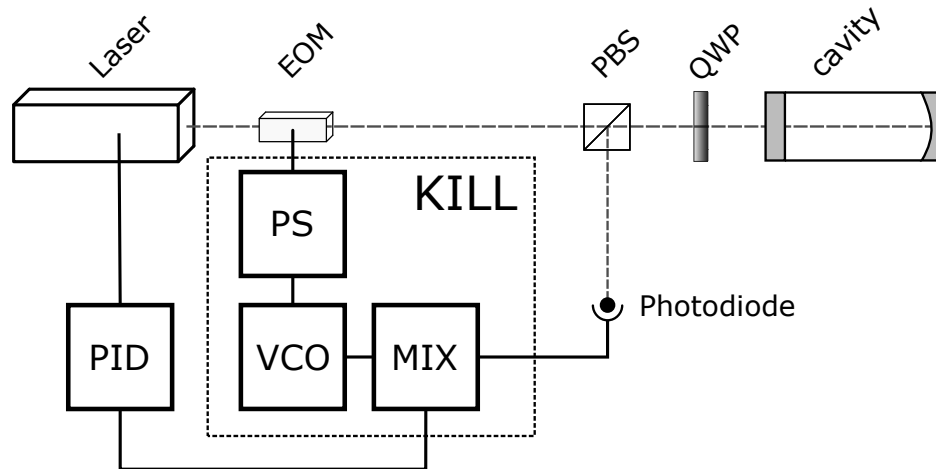


Figure 7: Schematic setups for the electronic requirements for PDH-locking using phase modulation. The example depicted shows phase modulation by using an electro-optic modulator (EOM) in the beamline. Alternatively, the diode current can be directly modulated in the laser, giving the same result.

Abbreviations: PS: Phase shifter, VCO: Voltage controlled oscillator, MIX: Frequency mixer, PID: PID controller, PBS: Polarizing beam splitter, QWP: Quarter-wave plate.

2 Electronics

This section shows the experimental work on different electronics needed for PDH-locking. First, the piezos which change the cavity length and shift the resonance frequency need high voltages to fulfill their purpose. The elements that go into an amplifier which can provide these voltages in a consistent, stable and adjustable way are described in subsection 2.1. In a separate part (2.1.1), I will give details about the piezoelectric elements we used, their characteristics and measurements we performed. Next, subsection 2.2 shows the design and choice of the locking electronics (KILL) and the considerations that go into it.

2.1 Piezo electronics

PDH-locking to a specific frequency requires the ability to adjust the resonance frequency of the cavity. Alternatively, one could use acousto-optic modulators for the same purpose. For this, one cavity mirror is glued to a piezo ring. As the piezo expands or contracts, the cavity length, and therefore the resonance frequency, is changed. This subsection goes into detail about the voltage generation needed for the piezos to fulfill this purpose. It also gives an overview over the parts needed to control the piezos and details about cooling of the driving electronics. A separate part is dedicated to characterization of the piezos to ensure they behave as expected and required. We use two differently sized piezos to mitigate effects of thermal expansion of the piezos, which is also discussed in subsection 2.1.1.

When applying a voltage difference across a piezoelectric material, it will expand or contract depending on the sign of the voltage and the strength of these effects depends on the absolute value of the voltage. The piezo rings we use have two silver electrodes, one on the inside surface of the ring and one on the outside, as depicted in Fig. 8 (a). Piezo dimensions are shown in Fig. 8 (b). In order to ensure that the resonance frequency can be adjusted over a wide enough range, i.e. ideally more than one free spectral range of the cavity, high voltages are needed. Thus we designed an electronics box able of supplying voltages between -400 V and +400 V. The voltage needs to be easily tunable and stable over the entire range. While tunable voltage supplies for low voltages are readily available or easy to build, for large voltages this is not the case.

The ± 400 Volts are generated using four 200 V linear power supply units (PSU)³ connected in series.⁴ All power supplies are set to output 208 V using the built-in potentiometers. This ensures stable voltages in the desired range of 200 V per PSU and that any boundary effects in the PSUs do not disturb the rest of the system. The output voltage is then generated using high power operational amplifiers⁵ (op-amps) used as inverting amplifiers (Fig. 10 (a)).

³IHB200-0.12, International Power

⁴When switched on, the op-amps and capacitors draw a lot of current, which resulted in a latch-up of the PSUs, effectively halving the voltage range to either the positive half or the negative one. We solved this in our setup by adding several large capacitors that will provide the necessary currents and installing a separate switch for the op-amp boards. The op-amps can then be switched on separately after waiting a few seconds after turning on the PSUs to allow the capacitors to charge. A schematic of the circuit can be found in Appendix B.1.

⁵PA94, APEX microtechnologies, manual link

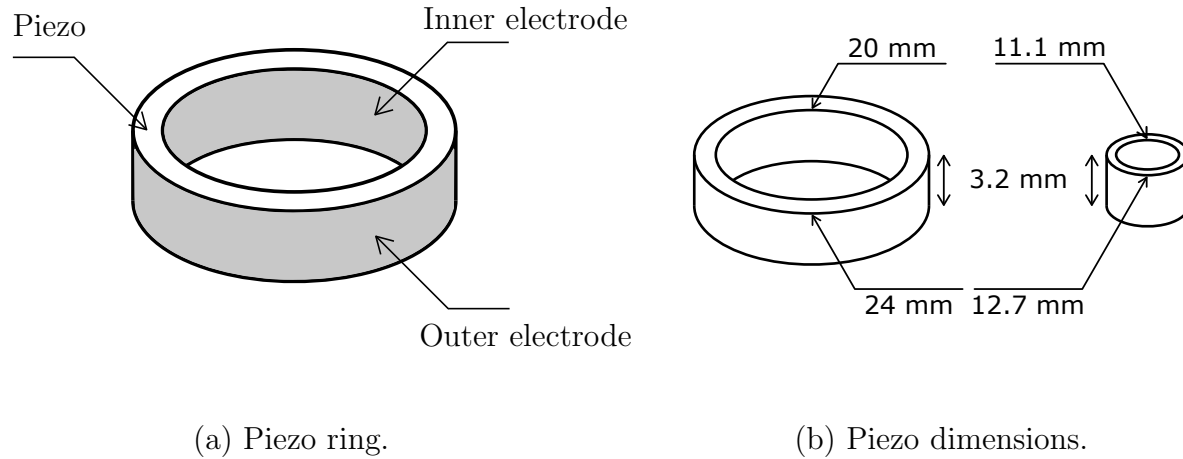


Figure 8: Panel (a) shows one of the piezo rings used. The ring expands or contracts along its cylindrical axis. Panel (b) shows the dimensions of both sizes of piezo rings used.

In this configuration, the op-amps amplify an input signal (between -10 and $+10$ V) by a factor of -40 , which results in an output range of ± 400 V. The amplification that the setup provides has been measured over the input range from -10 V to $+10$ V and the data can be seen in Fig. 9. The fitted amplification is -39.57 ± 0.01 and the y-axis offset is 0.20 ± 0.06 . The op-amps have a slew rate of $700 \frac{\text{V}}{\mu\text{s}}$ [22] which allows them to react quickly to changes in the input signal.

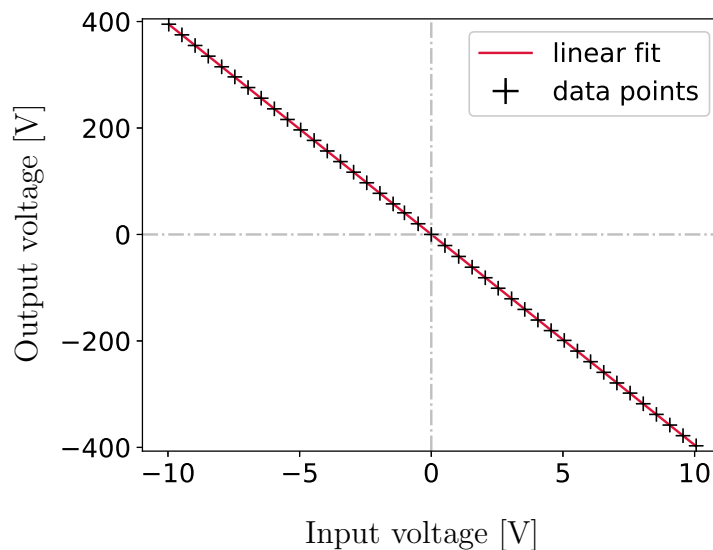


Figure 9: Plot of input voltage and output voltage of the piezo driver box. The amplification is almost perfectly linear over the whole range.

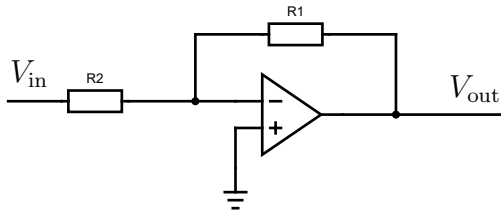
The input signal will be controlled remotely on a webserver hosted on a Raspberry Pi⁶, converted by a digital-analog-converter (DAC)⁷. The DAC outputs an analog signal, which is then amplified and supplied to the piezo electrodes. In this way the cavity length is easily tunable using a webserver interface to fit the required resonance frequency. In addition to the above elements, the raspberry pi, the DAC, its evaluation board and some cooling fans are powered by a ± 15 V PSU, all packed into a single 19" electronics rack. Pictures can be found in Appendix B.1.

Power supplies and especially the op-amps generate heat while running. Therefore the box needs to be cooled, otherwise parts may break or performance decreases. Each of the four op-amps (one for each cavity) is thermally connected to a heatsink via aluminum blocks as shown in Figure 10 (b). Internal power dissipation of the op-amps can be calculated using [22]

$$R = \frac{\Delta T}{PD + PD_Q} - 0.1 \frac{^\circ\text{C}}{\text{W}},$$

$$PD_Q = 0.024 \text{ A} \times V_{SS} = 0.024 \times 800\text{V},$$

where ΔT is the temperature difference between case and environment, PD is maximum power dissipation ($PD = 30 \text{ W}$ according to manufacturer), PD_Q is total quiescent power dissipation and V_{SS} is total supply voltage.



(a) Inverting amplifier.



(b) Heatsink.

Figure 10: Op-amps used as inverting amplifiers are connected as is shown in Panel (a). The input voltage (left-hand side) is amplified by a factor of $-\frac{R_1}{R_2}$. Panel (b) shows an op-amp connected to an aluminum block which makes thermal contact with the black anodized heatsink.

The heatsinks are rated for 2.0 K/W which theoretically keeps ΔT below 42°C . Additionally, two fans provide a constant flow of air from the front of the box to the back to provide additional cooling. At the time of writing this thesis, the piezo driving system has been running continuously for several weeks without issues.

⁶Raspberry Pi 3, Raspberry Pi Foundation.

⁷AD5371 on evaluation board EVAL-AD3571EBZ, Analog Devices, datasheet link

2.1.1 Piezo characterization

In our setup we use ring-shaped piezos that expand along the cylindrical axis when a voltage is applied. The rings have two silver electrodes on the inner and outer ring surfaces, as shown in Fig. 11 (a). The piezoelectric elements are glued to one mirror of each cavity and by expanding or contracting they change the cavity length and therefore control resonance frequencies of the cavities. The piezos we use are ceramic⁸ and we use two different sizes of rings for each cavity. In principle, one piezo per cavity is enough to change cavity length, but the cavity length is then very susceptible to temperature fluctuations since the piezo has a thermal expansion coefficient which can not be neglected. To cancel this thermal expansion we use two piezo rings of the same thickness: A smaller one to which the mirror is glued, and a larger one which is glued to the cavity casing such that the mirror stays at the intended position. On the other side, the two rings are connected by a macor ring which holds them in place and doesn't short the electrodes since macor is an electrical insulator. Since both piezos are the same thickness, they will expand or contract the same distances, leaving the mirror in the same place [23]. This setup is shown in Fig. 11 (b).

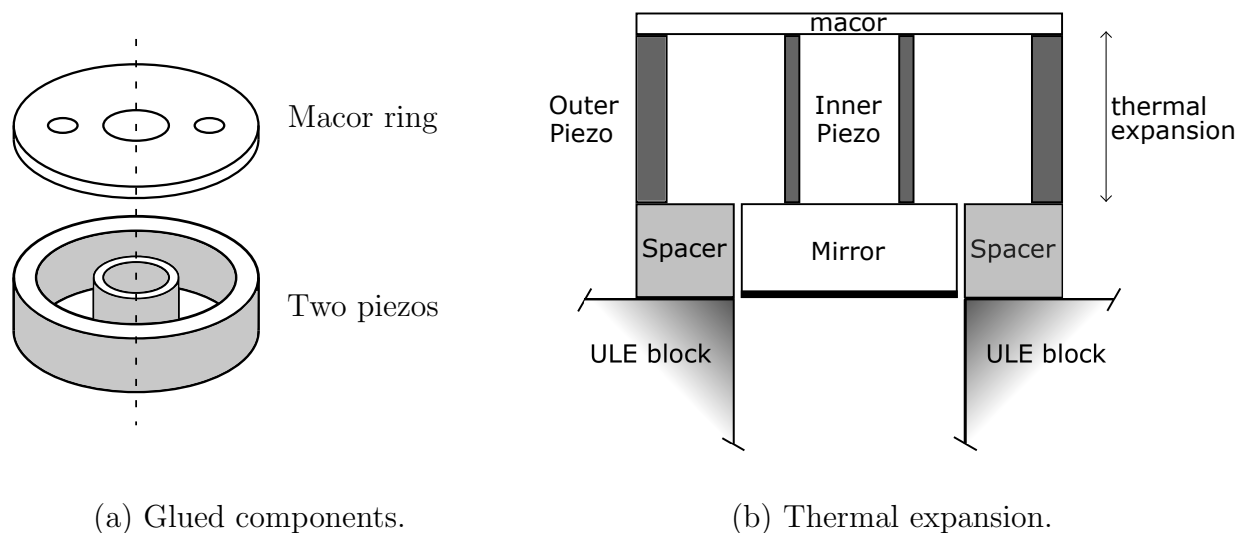


Figure 11: Panel (a) shows the two piezos glued together with the macor backplate. The holes in the macor are for wires that connect to the electrodes. Panel (b) illustrates how thermal effects on cavity length are mitigated by using two piezos instead of only one.

The distance the piezo expands or contracts per voltage applied across the material can be measured using a Michelson interferometer [14], see Fig. 12 (a). In such a setup, a beam is split into two beams using a 50/50 beam splitter. One of the paths after the splitter has a variable optical path length, here realized by moving one mirror with a piezo. The difference in optical path length between the two arms of the interferometer leads to interference upon recombination after reflection. Looking at the interference peaks (Fig. 12 (b)) on a photodiode and knowing the wavelength of the light, one can then determine the distance the piezo expanded. The measurement shown in Fig. 12 (b) was performed on a single

⁸Pz27 by Meggitt A/S, datasheet link

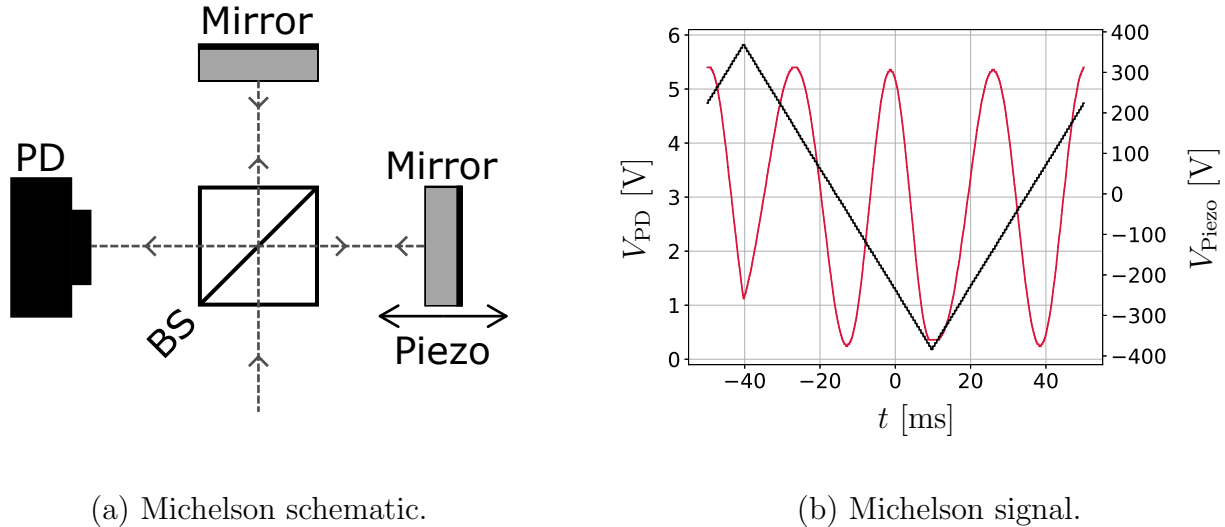


Figure 12: This figure shows a schematic of a Michelson interferometer (a) and the oscilloscope signal from such a setup (b). In the latter one can see interference peaks as the voltage changes. The plot in (b) is from using 866 nm light using one of the piezos with larger diameter and a height of 5 mm.

Abbreviations: PD: Photodiode, BS: Beam splitter.

piezo glued to a mirror in a Michelson interferometer. The piezo in this case has the same diameters as shown in Fig. 8 but its height is 5 mm instead of 3.2 mm. We measure a voltage response of $1.15 \pm 0.02 \frac{\text{nm}}{\text{V}}$. Scaling this result with piezo height, for the piezos used in the cavity setup, the response is $1.33 \pm 0.736 \frac{\text{nm}}{\text{V}}$, in agreement with results from [23]. Over the voltage range of 800 V, this leads to a range of 589 ± 16 nm for each of the larger piezo rings. This range can be increased by wiring the two piezos in opposite directions, such that if one expands, the other one contracts.

2.2 Locking electronics (KILL)

As described in section 1.4, PDH-locking needs various electronic elements to function. Specifics on the various parts and the how they are arranged in our setup are described in this subsection.

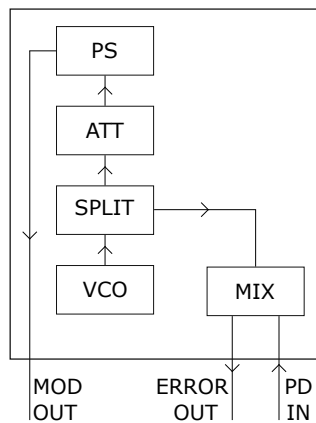
To reduce noise and cable delays, it is helpful to combine all possible elements on a single compact PCB to allow for fast processing of a reflection signal. Most of the elements such as VCOs or mixers are available as integrated circuits which are soldered onto the PCB⁹. To pick up cavity reflections the photodiode needs to be fast enough to pick up signals at the modulation frequency Ω .

The VCO¹⁰ in our setup provides the modulation signal between 100 and 150 MHz,

⁹The PCB was designed by Ben Keitch [21] and the version used here is 1.3.0, which introduces several improvements over the older 1.2.0 design such as the phase shifter, optional filter circuits and more potentiometers to adjust other parameters. Details can be found in App. ??.

¹⁰JTOS-150+, mini-circuits, datasheet link

tunable using a potentiometer. This signal is split using a power splitter¹¹ into two weaker signals, one that goes into the mixer and one that goes to a voltage controlled attenuator. The attenuator¹² is used for switching the modulation signal on and off while keeping everything else running. From the attenuator, the modulation signal goes into a phase shifter¹³ and afterwards to the laser¹⁴ or the EOM¹⁵, where it modulates the phase of the laser beam. The phase shifter is used for ensuring that the signal from the photodiode is in phase with the modulation signal coming into the mixer. This improves the quality and strength of the PDH-error signal coming out of the mixer¹⁶. The photodiode chosen was a free-space fast amplified photodiode¹⁷ with a bandwidth of 380 MHz. It is fast enough to reliably measure any modulation frequency the VCO can put out. Weak reflection signals may need to be further amplified using external amplifiers. Fig. 13 shows a schematic of the PCB with the layout of the aforementioned elements (a) as well as a picture of the assembled PCB (b). Schematics of the full PCB can be found in Appendix. B.2.



(a) PCB schematic.



(b) Picture of PCB.

Figure 13: A simplified schematic of the elementary components of a locking circuit is in panel (a). For comparison there is a picture of the full PCB in panel (b).

Abbreviations: PS: phase shifter, ATT: attenuator, SPLIT: power splitter, VCO: voltage controlled oscillator, MIX: mixer, PD: photodiode, MOD: modulation signal.

¹¹ADP-2-1+, mini-circuits, datasheet link

¹²RVA-2500, mini-circuits, datasheet link

¹³JSPHS-150+, mini-circuits, datasheet link

¹⁴DL pro, Toptica, with laser controller DLC pro.

¹⁵PM8-VIS, QUBIG, weblink

¹⁶TUF-3SM+, mini-circuits, datasheet link

¹⁷PDA015A, Thorlabs [24]

3 Optics

Section 3 is about the cavity as a frequency-reference and the optical setups needed for locking to it. The setup presented is intended for locking four different wavelengths at the same time in a compact way. Details about the cavities and an overview over their properties is given in subsection 3.1. In order to get good enough coupling of light into a cavity to allow for locking, optical elements are needed to transform the beam. The necessary steps and parts for this are described in subsection 3.2.

3.1 Cavity design

In this setup we use four cavities for four different wavelengths. Using them for locking requires a setup which reduces any perturbations to a minimum, which is realized with low thermal expansion materials and by placing the cavities in a vacuum chamber. The design of the cavities themselves need to take wavelength-dependent properties of mirror coatings into account and the cavity needs to allow for a sufficiently narrow lock of each ion transition. Also, the assembly of the four cavities is described in detail in this subsection.

Cavities used for frequency stabilization need to be very stable over time. Otherwise, the utility of locking is greatly diminished as its purpose is to eliminate frequency drifts as much as possible. To reach this stability, we use materials with low thermal expansion coefficients, so-called ULE glass to house the cavity mirrors. All four cavities are compactly contained in a single block of ULE glass, which is then put into a vacuum chamber to further isolate the cavities from thermal and vibrational effects. The setup is shown in Fig. 14 (b).

As the reflective coating of the mirrors has different reflectivities at different wavelengths, the finesse is also implicitly wavelength-dependent. The mirrors implemented in the setup are supplied by thorlabs and use their standard coatings E02 and E03¹⁸. Their reflectivities at the different wavelengths and the resulting cavity properties are listed in Table 2. More details can be found in Appendix A.

λ [nm]	R1 (flat)	R2 (curved)	$\Delta\nu_{\text{FSR}}$ [MHz]	$\Delta\nu_{\text{FWHM}}$ [MHz]	\mathcal{F}	Coating
397	0.991	0.991	1499	4.31	348	E02 (blue)
423	0.995	0.995	1499	2.39	627	E02 (blue)
854	0.997	0.997	1499	1.38	1082	E03 (red)
866	0.996	0.996	1499	1.15	1307	E03 (red)
732	0.994	0.994	1499	2.87	522	E02 (blue)

Table 2: Cavity properties at the four wavelengths they will be used at. Note that the cavities for 397 nm and 423 nm are identical and all differences arise from wavelength-dependent mirror properties. The same holds for 854 nm and 866 nm. All cavities are the same length, $L = 100$ mm Curved mirrors each have a radius of curvature $R = 200$ mm.

¹⁸Thorlabs, Reflectance plots and data, weblink

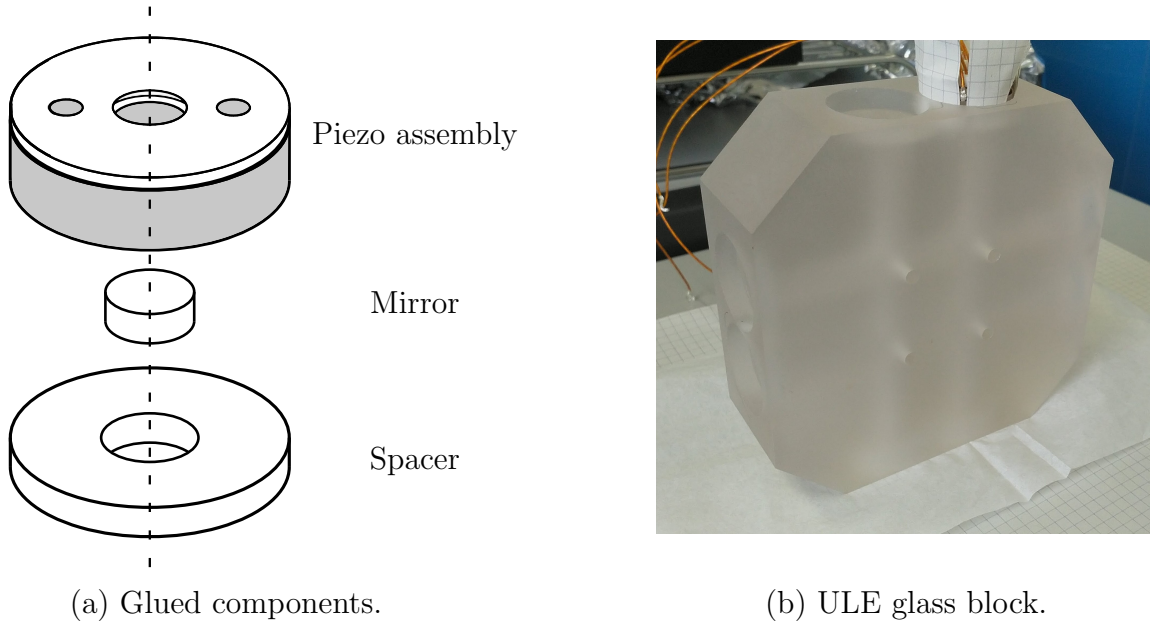


Figure 14: Schematic of the elements glued together is shown in panel (a). A photo of the ULE glass block during gluing preparation is shown in panel (b).

All components are glued to each other using a low-outgassing epoxy glue¹⁹, such that the vacuum is compromised as little as possible. The curved mirrors are all glued directly to the ULE block, while the flat mirror is attached to the smaller piezo ring, as shown in Fig. 14 (a). The larger piezo is then glued to a glass spacer of the same material thickness as the mirror such that the cavity has the intended length. The ULE glass block (Fig. 14 (b)) is designed to have cavities of length $L = 10$ cm. The gluing process is described in detail in Appendices C.1 and C.2.

3.2 Optics setup and mode-matching

Since cavities only allow coupling into certain cavity modes and strong coupling is needed for a consistent lock, mode-matching of the laser beam into the cavity needs to be optimized. This subsection looks at possible reasons for weak coupling and how coupling can be optimized using optics and principles from Gaussian optics.

The modes of a cavity are determined by the geometry of the cavity in question. For a Gaussian beam to couple into a cavity mode in a hemispherical cavity, the beam curvature $R(z)$ (see eq. (5) in section 1.2) has to match the mirror curvature at the curved mirror. Also, at the flat mirror, the curvature needs to be infinite, which means that the minimal waist w_0 needs to be located at the flat mirror. In our setup, the curved mirrors are all spherical with a curvature radius of $R = 200$ mm, the cavities are all $L = 100$ mm long and we try to couple into the cavity from the side with the flat mirror²⁰. These constraints give

¹⁹353ND, EPO-TEK, datasheet link

²⁰This ensures that the reflection is parallel to the incoming beam, facilitating alignment.

us the desired Rayleigh range and therefore also the mode beam waist

$$\begin{aligned}
 R(L = 100 \text{ mm}) &= 200 \text{ mm} , \\
 \Rightarrow z_R &= \frac{R}{2} = 100 \text{ mm} , \\
 \Rightarrow w_0 &= \sqrt{\frac{\lambda R}{2\pi}} .
 \end{aligned}
 \tag{22}$$

The constraint of the beam waist w_0 being located at the flat cavity mirror means that a focusing lens should be placed a focal length in front of the flat mirror. If the focus of the beam is in front of the mirror or inside the cavity, the beam curvatures at both mirrors will be mismatched, weakening coupling. However, even when the focus is correct, the waist of the beam can be different from the ideal waist (eq. (22)). A laser beam can be resized using a telescope made of two lenses. This should be positioned somewhere before the focusing lens. The beam waist also depends on the mode-field diameter in the fibre and the collimator that is used. In addition to these considerations, one has to take into account beam propagation in free space over the entire optical path. A Gaussian beam's waist and curvature change along the beam path even without any optical elements changing them. However, the beams we typically use in this setup are large enough that these effects amount to only small changes and are negligible in this case. The quality of a Gaussian beam and its spatial evolution along the beam path can and should be observed with a beam profiler. This way, one can find experimental deviations from the theoretical beam properties²¹.

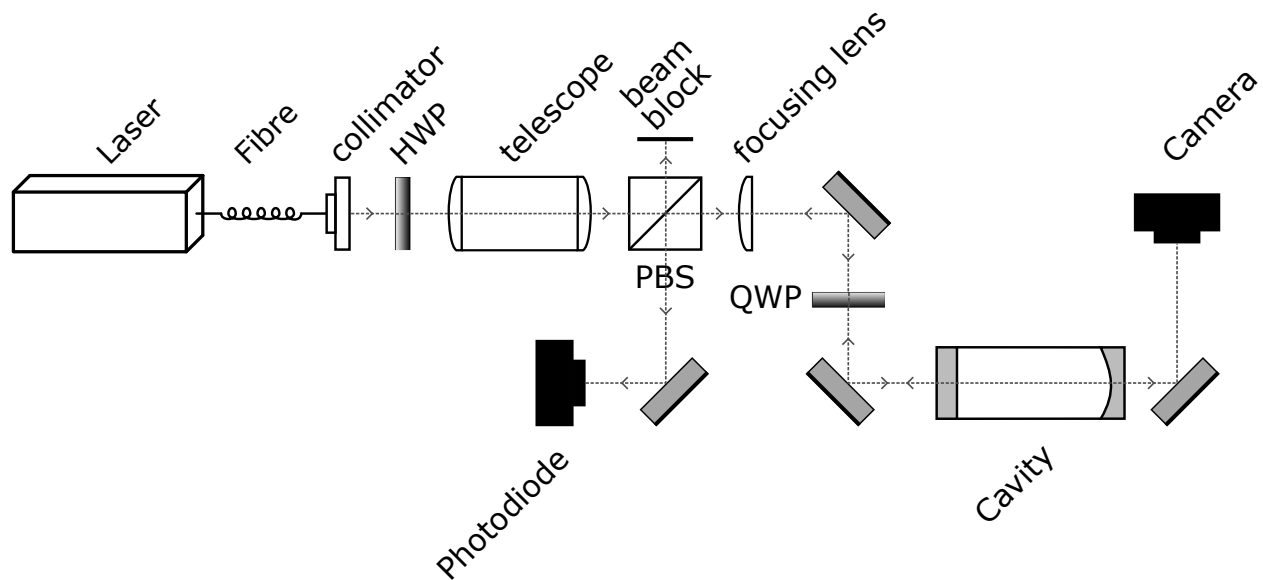


Figure 15: Setup of all optical elements used to optimize coupling and mode-matching into the cavity.

Alignment of the optics can be a difficult and time-consuming task. Mode coupling is very dependent on the alignment of the beam path with the cavity axis. If the beam hits

²¹Beam profiling is also a mechanism to check for any errors made in setup such as wrong focal length lenses or broken collimators and fibres.

the cavity off-center or at an angle, mode coupling is severely decreased [13]. The beam's position on the in-coupling mirror can only be checked and improved by walking the beam while constantly looking at the transmitted or reflected intensity. Here, we found that for weak coupling, the transmission is easier to look at. The angular alignment is best determined by looking at the back-reflection from the in-coupling mirror and checking that it overlaps as well as possible with the incoming beam²². More details on the alignment procedure can be found in Appendix C.3. A complete setup is sketched in Fig. 15.

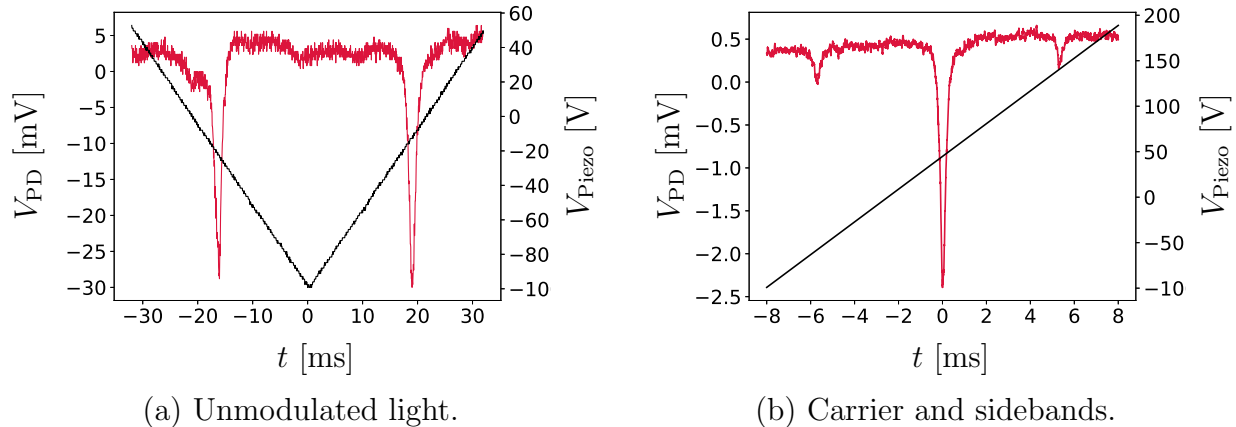


Figure 16: Reflected intensity of 397 nm light on resonance with a cavity. Photodiode signal is in crimson (left scale), piezo driving voltage is in black (right scale). Panel (a) shows resonance peaks of unmodulated light. The negative voltage on the photodiode is due to using AC-coupling on the oscilloscope to record the data. The modulated case is shown in panel (b) with sideband dips to the right and the left of the carrier dip. In (b) the voltage (black) has been linearly fitted. Both plots have been smoothed with an order 3 Savitzky-Golay filter to improve signal-to-noise ratio on the reflection signals.

Once good mode-coupling is achieved, the reflected light shows clear dips in power when measured with a photodiode. For unmodulated light, this is shown in Fig. 16 (a). For modulated light with known modulation frequency $\frac{\Omega}{2\pi} = 109.55$ MHz, the same is shown in Fig. 16 (b). This is the optimal frequency for the EOM we used²³. From the latter, we can use the known modulation frequency to calculate the full-width-half-maximum linewidth of the cavity. We used one of the blue cavities with E03 coating and 397 nm light for this measurement. The results are a cavity linewidth of $\Delta\nu_{FWHM} = 4.6 \pm 0.4$ MHz and a finesse of $\mathcal{F} = 321 \pm 25$. Which is close to agreeing with the theoretically predicted values in Table 2. The lower finesse can be due to errors in the gluing of the cavity and other experimental deviations from the ideal setup.

Using the reflection from the modulated beam, one can also determine the frequency range the piezo assembly can cover. A plot of carrier and sideband reflection dips can be

²²This is easier for flat mirrors since the reflected angle does not depend on the beam position on the mirror. Therefore one can independently optimize angular and translational alignment. For curved mirrors, this is not the case.

²³PM8-VIS, QUBIG, weblink

found in Fig. 16 (b). The voltage difference between a sideband reflection dip and the carrier reflection dip lets us calculate this frequency range. The effective range of the two piezos wired in opposite directions amounts to 876 ± 4 MHz change in resonance frequency, significantly less than a free spectral range of $\Delta\nu_{FSR} = 1500$ MHz. In our setup, the piezos should be able to expand over a larger range, as is also shown in section 2.1.1. The cause of this issue is likely glue expanding into the space between mirror and spacer during curing. The glue partially holds the mirror to the spacer, hindering its movement when the mirror is displaced by the piezo expansion. This issue can be fixed by disassembling the cavity and carefully regluing everything. The spacer ring can also have a larger hole to further reduce the chance of gluing the mirror to the spacer.

The modulated reflection signal can then be fed into the KILL box where it gets mixed with the modulation signal. The resulting PDH-error signal can also be displayed on an oscilloscope, shown in Figure 17.

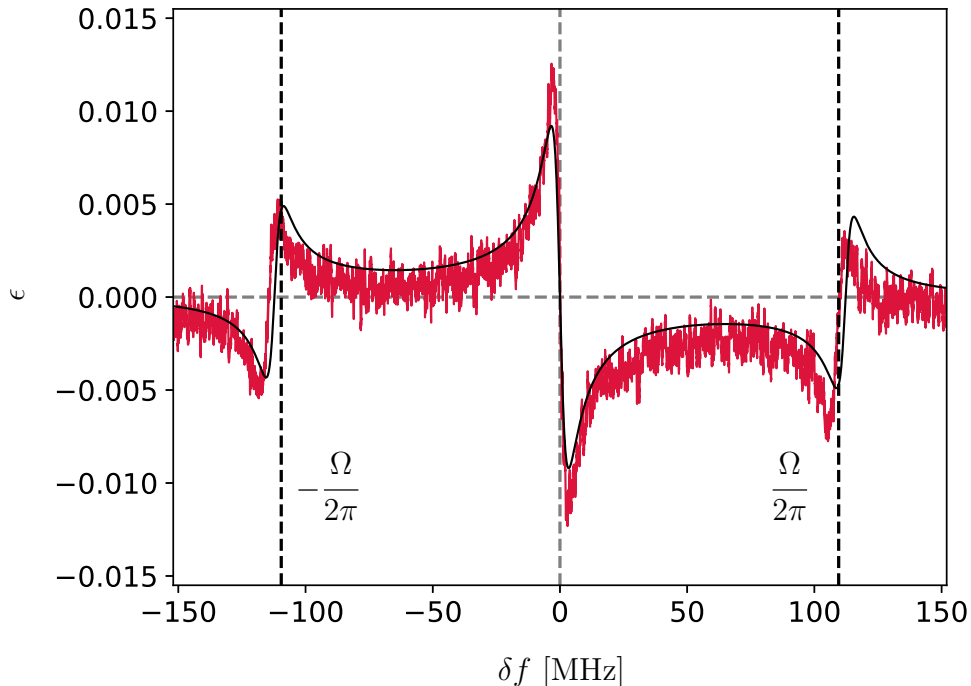
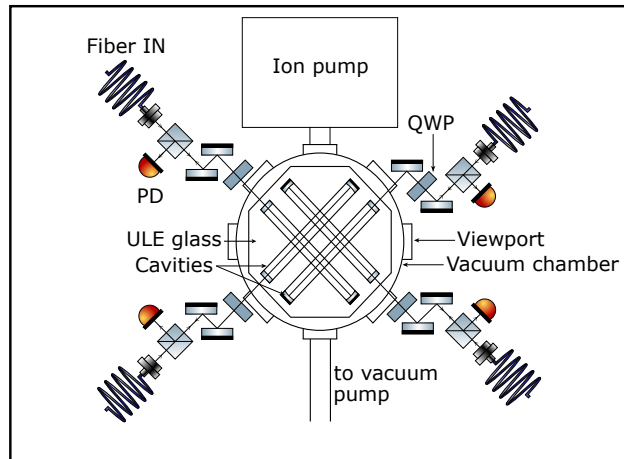
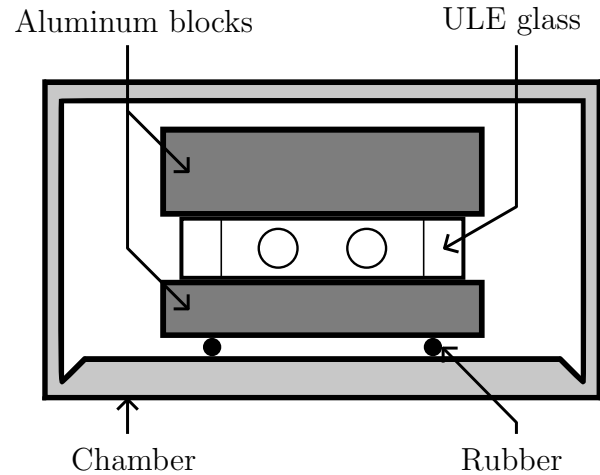


Figure 17: PDH error signal of 397 nm light, modulated at $\frac{\Omega}{2\pi} = 109.55$ MHz with an EOM (black dotted lines). Data (crimson) was filtered during measurement on the oscilloscope (6 kHz noise filter) and then smoothed using a Savitzky-Golay filter (order 3) to improve signal-to-noise ratio. Then data was fitted with a PDH error signal, see eq. 17 (black).

The combined optics setup for four cavities fits on a single 600×600 mm breadboard as depicted in Fig. 18 (a). The four cavities are glued to the ULE glass block in such a way that on each side of the block, one beam is coupling into a cavity. The ULE glass block will be put directly on a block of aluminum to ensure that any thermal gradients are quickly balanced out, since aluminum is a good conductor of heat. Another aluminum block



(a) Breadboard schematic.



(b) Vacuum chamber cross-section.

Figure 18: Schematics of the breadboard including optics for all four cavities and vacuum elements (a) and for the mounting of the ULE glass block inside the vacuum chamber (b).

will be put on top of the glass block for the same purpose and also to hold the block in place using friction. This ensemble will then be put inside a vacuum chamber, separated from the chamber bottom using small vacuum-compatible rubber pieces. Additional rubber pieces are wedged between the walls and the aluminum block. The rubber provides both weak thermal contact between the chamber walls and the aluminum block as well as keeping the block from moving around inside the chamber. A sketch of this setup can be seen in Figure 18 (b). After the chamber is evacuated, the only thermal contact from the cavities to the environment is via the rubber pieces connecting the bottom aluminum block to the bottom of the chamber.

4 Summary and Outlook

This thesis shows the process of designing and implementing a laser-locking system capable of locking four different wavelengths simultaneously. The setup consists of four optical cavities combined in a ULE glass block to keep them stable from thermal fluctuations. The cavities serve as frequency references for a PDH-locking system that transfers the stability of the cavities to the less stable lasers.

The thesis also describes the design of a ± 400 V piezo driver. The locking electronics are combined on a single PCB in eurocard format using integrated circuits. The hemispherical cavities are assembled by gluing mirrors to the ULE glass block using epoxy glues. Laser light has been coupled into the cavities well enough to produce a PDH error signal. Phase modulation of the laser light is achieved using an EOM modulating at 109.5 MHz. The reflection from the cavity makes it possible to measure cavity properties. We were able to confirm the theoretical values for finesse and linewidth of one of the cavities experimentally.

The cavity resonance can be adjusted using the piezos. Over the total driving range of 800 V, the resonance frequency can be shifted by about half a free spectral range. This is not enough to be able to choose any arbitrary resonance frequency. The reduced range is likely due to glue expanding during curing and partly gluing the mirror in place. Therefore the mirror can't be freely moved by the piezos and that causes the reduced range.

However, the results achieved can still serve as a proof that, aside from piezo range, all aspects of PDH-locking work in this setup. After the cavity is reassembled avoiding the gluing problem, the PDH-signal can be tried to lock to using a PID controller, which has not been implemented and tested yet. The cavities can also be placed inside a vacuum chamber to further stabilize them against thermal and mechanical noise.

Acknowledgements

Many people have been tremendously helpful in doing this thesis. First of all, I want to thank Prof. Jonathan Home for allowing me to do research in his group and for his advice. Next to Roland Matt, who provided me with everything I need and for sharing his experience with optics with me. His advice has been invaluable and he always had time when I needed to discuss something. Thanks also to Robin Oswald, who introduced me to the world of electronics and who had many solutions and work-arounds at the ready when we needed them. And also for proof-reading this thesis and spending a lot of time assisting me with writing. I want to further thank Kunal Helambe for his help with experiments and assisting me with acquiring data for this thesis. Then also to Dr. Chris Axline, who helped me with his experience in inventor and with ordering and many other administrative things. Many thanks go out to Oliver Wipfli and Chiara Decaroli for their help with cavities and mode-matching and many interesting discussions. Last, I want to thank everyone in the TIQI group for welcoming me warmly when I started and for the lively atmosphere they create every day in the group.

5 References

- [1] D. P. DiVincenzo, “The physical implementation of quantum computation,” *Fortschritte der Physik*, vol. 48, no. 9-11, pp. 771–783, 2000.
- [2] J. I. Cirac and P. Zoller, “Quantum computations with cold trapped ions,” *Physical Review Letters*, vol. 74, no. 20, pp. 4091–4094, 1995.
- [3] R. Blatt and D. Wineland, “Entangled states of trapped atomic ions,” *Nature*, vol. 453, p. 1008, 2008.
- [4] H. Häffner, C. F. Roos, and R. Blatt, “Quantum computing with trapped ions,” *Physics Reports*, vol. 469, no. 4, pp. 155–203, 2008.
- [5] M. A. Nielsen and I. L. Chuang, *Quantum Computation and Quantum Information: 10th Anniversary Edition*. Cambridge: Cambridge University Press, 2010.
- [6] F. Leupold, *Bang-Bang Control of a Trapped-Ion Oscillator*. PhD thesis, ETH Zürich, 2015.
- [7] D. M. Lucas, A. Ramos, J. P. Home, M. J. McDonnell, S. Nakayama, J. P. Stacey, S. C. Webster, D. N. Stacey, and A. M. Steane, “Isotope-selective photoionization for calcium ion trapping,” *Physical Review A*, vol. 69, no. 1, p. 012711, 2004.
- [8] H. Metcalf and P. van der Straten, *Laser Cooling and Trapping*. Springer New York, 2001.
- [9] A. Siegman, *Lasers*. University Science Books, 1986.
- [10] O. Svelto, *Principles of Lasers*. Springer US, 2010.
- [11] L. Allen, M. W. Beijersbergen, R. J. C. Spreeuw, and J. P. Woerdman, “Orbital angular momentum of light and the transformation of laguerre-gaussian laser modes,” *Physical Review A*, vol. 45, no. 11, pp. 8185–8189, 1992.
- [12] G. Hernandez, *Fabry-Perot Interferometers*. Cambridge University Press, 1988.
- [13] D. Z. Anderson, “Alignment of resonant optical cavities,” *Applied Optics*, vol. 23, no. 17, pp. 2944–2949, 1984.
- [14] E. Hecht, *Optics*. Pearson, 5th ed., 2016.
- [15] R. W. P. Drever, J. L. Hall, F. V. Kowalski, J. Hough, G. M. Ford, A. J. Munley, and H. Ward, “Laser phase and frequency stabilization using an optical resonator,” *Applied Physics B*, vol. 31, no. 2, pp. 97–105, 1983.
- [16] R. W. P. Drever, G. M. Ford, J. Hough, I. M. Kerr, A. J. Munley, J. R. Pugh, N. A. Robertson, and H. Ward, “A gravity wave detector using optical cavity sensing,” *Proceedings of the Ninth International Conference on General Relativity and Gravitation, Jena, July 1980*, p. 265–267, 1980.

-
- [17] R. V. Pound, “Electronic frequency stabilization of microwave oscillators,” *Review of Scientific Instruments*, vol. 17, no. 11, pp. 490–505, 1946.
- [18] D. Colton and R. Kress, *Inverse Acoustic and Electromagnetic Scattering Theory*. Springer Berlin Heidelberg, 1997.
- [19] E. D. Black, “An introduction to pound-drever-hall laser frequency stabilization,” *American Journal of Physics*, vol. 69, no. 1, pp. 79–87, 2001.
- [20] P. Horowitz and W. Hill, *The Art of Electronics*. Cambridge University Press, 2015.
- [21] B. Keitch, *A Quantum Memory Qubit in Calcium-43*. PhD thesis, Oxford, 2007.
- [22] APEX-microtechnologies, *High Voltage Power Operational Amplifiers PA94 manual*.
- [23] F. Lindenefelser, *Laser stabilization for quantum information experiments with trapped ions*. Master, ETH Zürich, 2011.
- [24] Thorlabs, *PDA015A/(M) Si Amplified Detector User Guide*.

Appendices

A Mirror reflectivity plots

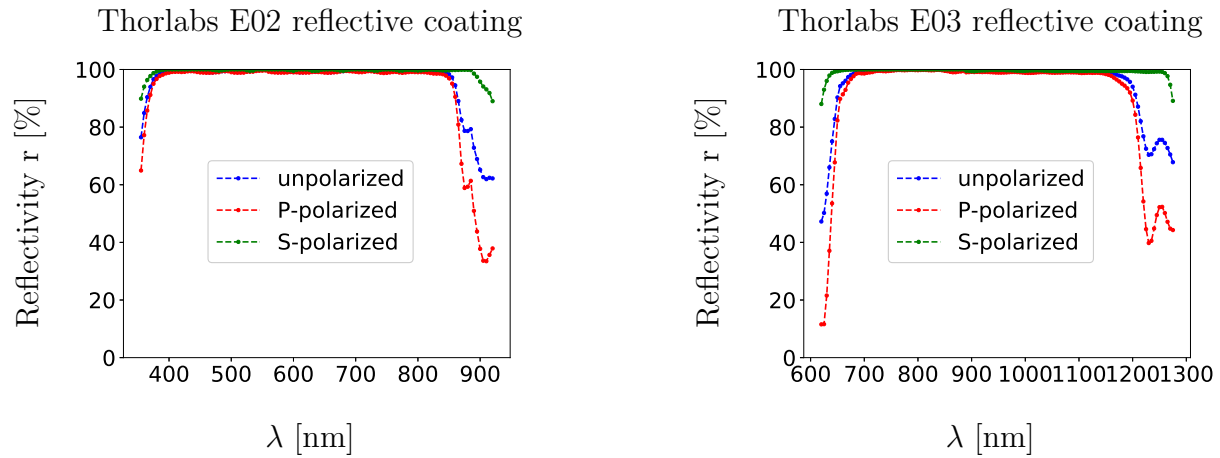
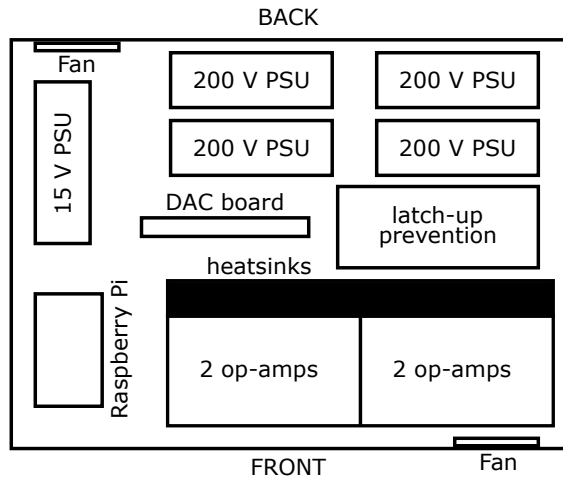


Figure 19: Reflectivity plots provided by Thorlabs at 45° angle of incidence for different polarizations²⁴.

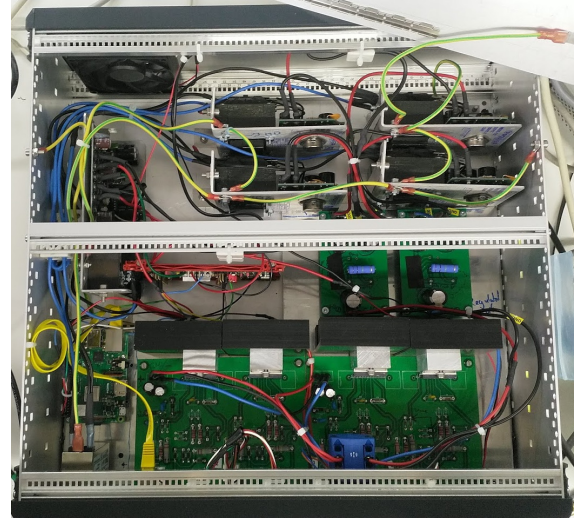
²⁴Thorlabs reflectance plots and data, weblink

B Electronics schematics

B.1 Piezo driving



(a) Schematic.



(b) Photo.

Figure 20: Topdown view onto the piezo driver box. The 15 V power supply powers both fans, the Raspberry Pi and the DAC board. The Raspberry Pi can be accessed via the ethernet port on the front panel.

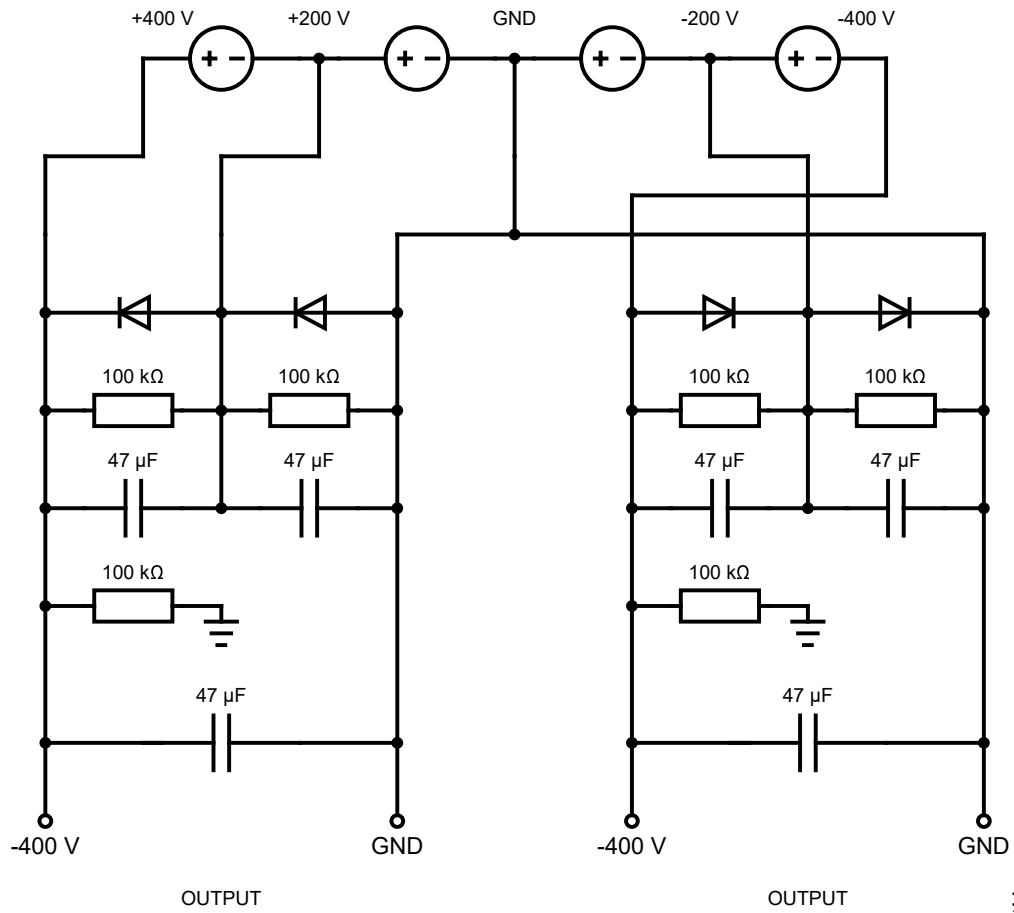
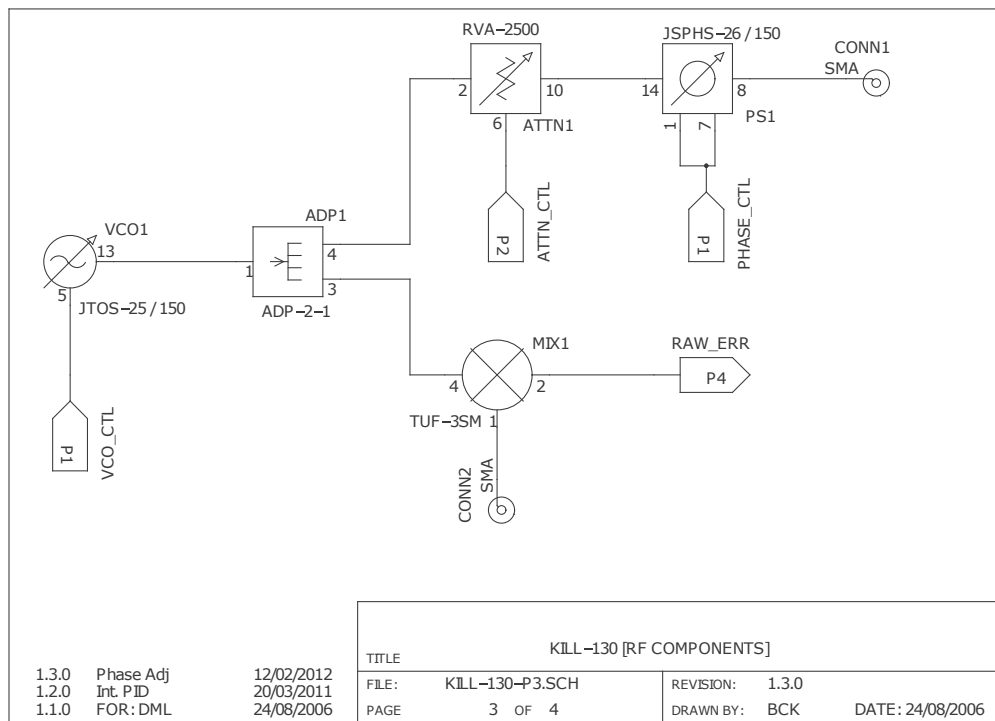
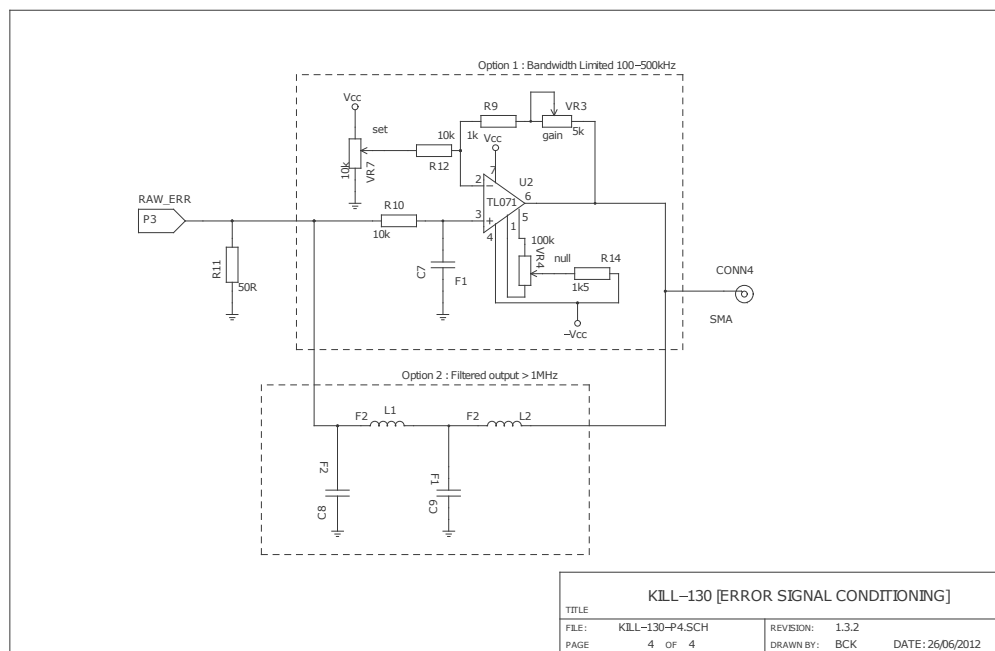


Figure 21: Latch up circumvention circuit including PSU. This part of the system is separated from the op-amp boards with a rotary switch. After turning it on, the capacitors need a few seconds to charge before connecting them to the op-amps using the switch.



(a) RF components.



(b) Error-signal.

Figure 23: Electronic circuit diagram of the RF circuitry and error-signal conditioning for KILL version 1.3.0, designed by Ben Keitch.

B.3 Problems with KILL version 1.3.0

- Push-pull stage consisting of transistors Q1 and Q2 (see Fig. 22 (b)) has wrong footprint on the PCB. For both, collectors and emitters are switched, so the transistors need to be soldered onto the board flipped on their heads. This was fixed in version 1.3.1.
- Error signal conditioning happens on the output of the frequency mixer. There are two options that can be chosen (see Fig. 23 (b)), the circuit doesn't work if both options are implemented simultaneously. We always went for the simpler option 2, but we shorted the contacts for inductors L1 and L2. We used an external low-pass filter to achieve the same purpose²⁵.
- We had problems with regulator VREG1 (see Fig. 22 (a)), where the output voltage varied between 11.7 V and 13 V between different specimens. This has a direct impact on the power of the modulation signal, where higher voltage results in higher output power. This is also a way to increase modulation power, if it is too weak.

²⁵NLP-1.9+, mini-circuits, datasheet link

C Procedures

C.1 Wire gluing

For the piezo wiring we used kapton-insulated copper wires²⁶ and glued them to the piezo electrodes using a conductive glue²⁷.

Notes on the oven: If you glue glass blocks or other fragile things, leave the oven cold until you put the object in to make sure nothing gets damaged from sudden heating up. The oven itself heats quite slowly. If you just glue aluminum pieces or other similar things, you can preheat the oven before gluing to save time and put the object into the oven when it's already hot.

1. Prepare the necessary tools: Something to mix the glue on (e.g. bottom of a small petry dish), a mixing tool (e.g. piece of wire or spatula), the glue components, wipes, acetone for cleaning, a scale, aluminum foil or another clean surface and gloves.
2. Wear gloves when handling glue, otherwise you get it on your hands and spread it to unwanted places. Prepare a clean surface (e.g. using aluminum foil) to work on where you have enough space for all your tools. Ideally work close to the oven so you don't have to move the glued objects across the room to reduce the chance of moving glued things before the glue can cure.
3. Mix the glue components. Use a scale for measuring the weights to get the right mixing ratio. Since we are working with very small amounts close to the error bar on the scale, the ratio might be off, but it is not that crucial. Just try to get close to the recommended ratio.
4. Always clean the surfaces to be glued with acetone/isopropanol to make sure the glue can stick properly.
5. Once the glue is mixed and the surfaces are clean, use a small tool (wire, spatula, ...) to apply the glue to the correct electrode in a small drop. Make sure to not short the electrodes with glue!
6. Put the wire (degloved!) into the glue and fixate it somehow with tweezers, tape, clamping, ... If you don't fixate the wire it will probably move or come off.
7. Put the object in the oven at the recommended temperature and let it cure for the recommended time. For H21D this is at 150°C for 1 hour.
8. Once the glue has cured, take out the item (careful!) and let it cool down. If the object is fragile (glass block or similar), leave it in the oven and just open the oven door a bit to let it cool down slowly.
9. Once the object has cooled down to room temperature, check if the gluing worked by tugging on the wires carefully. Check for electrode shorts using a multimeter.

²⁶311-KAPM-075, Allectra, catalog weblink

²⁷H21D, EPO-TEK, datasheet link

C.2 Mirror gluing

The gluing steps are the same for the mirrors as they are for the wires. Here, the glue 353ND by EPO-TEK, which is a non-conductive epoxy glue. The differences from wire gluing are that mirrors are held in place by gravity, so one should prepare a mount such that the mirror lies completely flat on the surface. In order to keep the mirrors centered in the holes, which are larger in diameter, one can use small pieces of paper or foil as spacers wedged between the hole and the mirror all around the hole. Usually, 3 or 4 pieces are good enough. Try to not put the paper all the way down to reduce the chance of the paper being glued. Since the glue spreads a bit during curing, this might not be completely avoidable. After gluing, check alignment of the mirror and take out the paper/foil spacers as completely as possible.

C.3 Beam alignment and mode-matching into cavity

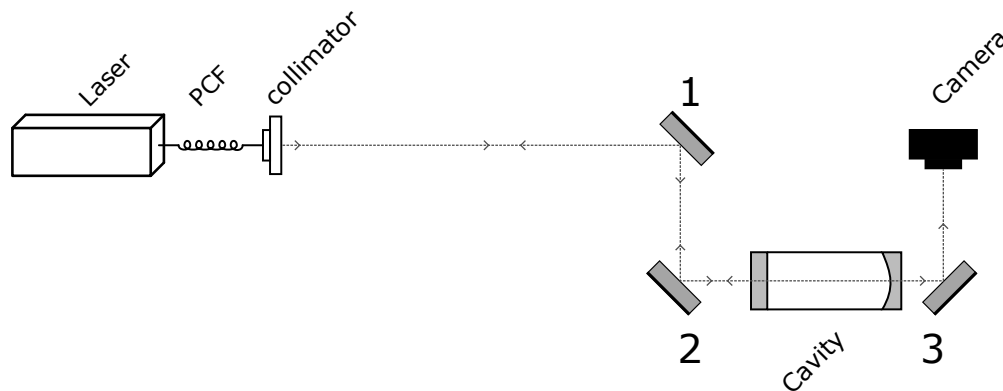


Figure 24: Setup for aligning the beam into the cavity.

1. Begin with only mirrors in place, remove all other elements such as lenses, waveplates, etc. This makes it easier to align and gives you the most power in the beamline. So start with only the collimator, mirrors 1 and 2, and the cavity in place.
2. Roughly align collimator and mirrors by hand such that the beam hits the mirrors at $\tilde{45}^\circ$ and it hits the cavity such that you can see the reflection.
3. Check by eye whether you hit the cavity in the center and correct using mirror 1 if it doesn't hit the center.
4. Overlap the reflection with the incoming beam using mirror 2 at all points along the beamline.
5. Repeat the last two steps until the beam hits the center and the reflection overlaps well.
6. At this point, there should be some coupling into the cavity. Start scanning the cavity or the laser frequency to check. Transmission will be weak so it might not be visible by eye, use a camera in transmission.

7. If you don't see anything, try adjusting the scan range and speed. The most likely modes you will see are some weird high order modes, so watch the camera very carefully. In my experience it's easiest if the scan frequency is slow (≤ 1 Hz) and the range small. Then adjust the scan offset over a wide range while watching the camera. Eventually you should see something if the reflection overlaps.
8. Once you see something, walk the beam with mirrors 1 and 2 to try and improve the modes you see. Regularly adjust the scan range to see if better modes appear.
9. Once you optimized the mirrors, start putting in all other optics you need. Use cage systems for lenses and the telescope. Waveplates don't change the beamline, but lenses and beam splitters do, so after putting in a lens or a splitter, reoptimize the mirrors to get bright modes.
10. Rotate the half-waveplate to get the maximum power possible through the PBS. Watch the reflection and rotate the quarter-waveplate to increase the power going to the photodiode.
11. Try adjusting lens position and telescope separation to improve mode-matching. This is only feasible when using cage systems, otherwise you will ruin the alignment every time you move a lens.